



**Fermilab**

TM-1391  
2872.000

THE NCI DICHROMATIC BEAM TESTS

L. Stutte

March 1986

THE NCI DICHROMATIC BEAM TESTS

Linda Stutte

March 11, 1986

INTRODUCTION

The new dichromatic train<sup>1</sup> was designed to meet a variety of goals:

1. Reach secondary beam momenta up to 750 GeV ( $x_F=3/4$ ).
2. Dump the non-interacting fraction of the primary proton beam cleanly in external dumps at all secondary momenta.
3. Reduce the wide-band background component of the beam as much as possible (better or at least as well as the old beam).
4. Obtain an energy resolution  $dE/E$  approximately 10% at all secondary momenta for radii up to one meter in the neutrino detectors.
5. Obtain the highest flux of secondaries possible while keeping the momentum bite of the beam at approximately 10%.
6. Contain the physical size (both longitudinal and transverse dimensions) of the beam layout in order to minimize costs.

As in all design efforts, some parameters must be optimized at the expense of others. The NCI design was chosen to emphasize increased flux as the most important of the above list, since, even with large mass detectors, the event rates are limited to a few events per pulse. (See Figure 1, which gives event rates at 1 TeV, as a function of secondary momentum selected.) As a consequence, wide-band background rejection and energy resolution at the detectors are not optimum, but are still within the design goals.

A conceptual layout of the NCI dichromatic beam is shown in Figure 2. All magnets used in the beam have large apertures (6-3-120 dipoles, and 4-Q-120 and 8-Q-32 quadrupoles) in order to obtain the maximum possible flux.

The beam bends in both the horizontal and vertical planes in order to minimize wide band background; the secondaries only point toward the neutrino detectors when momentum and sign selection are complete.

The first bend after the target (8.67 mr) and the length of drift spaces determine the maximum momentum acceptance of the train, which is about 15%. This parameter was chosen to maximize flux, while still maintaining reasonable energy resolution at the neutrino detectors. The production spectrum at higher secondary momenta reduces the momentum bite of the

beam to about 8% at 600 GeV.

Beam defining liners<sup>2</sup> are installed in the first two dipoles after the target. These liners, along with the two collimators shown in the figure, are used to remove off-axis particles which contribute to the divergence of the beam. It is important to minimize the beam divergence in order to provide good energy resolution at the neutrino detectors, and to insure that secondary particle fractions can be measured for a flux determination, using Cerenkov counter techniques.

A large engineering effort went into the design and construction of two 70 ton dump modules<sup>3</sup>, to contain the non-interacting fraction of the primary proton beam. These dumps had to be large enough to prevent ground water activation, and to protect workers who may have to work on near-by equipment; but also had to be transportable, since other neutrino beams may be installed in the target hall.

The NCI dichromatic train was assembled in 1983, and installed in Enclosure NW1 for the first 800 GeV run of the Tevatron, in order to get a first look at the properties of the train<sup>4</sup>. For most of this run, the train was used to provide a passive transport for the primary beam to the NWest test beam production target. Some 60 hours were scheduled for dichromatic tests in order to measure the momentum bite and the

angular divergence of the train. Accelerator performance and other equipment failures allowed only a fraction of this test time to be obtained. The results of those measurements are detailed in the following sections.

Figure 3 shows an overall layout of the equipment used for the tests. Intensity information was obtained from a SEM<sup>5</sup> placed in the primary proton beam upstream of the target, and from a large ion chamber<sup>6</sup> placed downstream of the train in the secondary beam. Primary beam shape and position were monitored with SWICs (segmented wire ion chambers) located at the entrance to the target hall (2 mm wire spacing) and just in front of the target (1/4 mm wire spacing). The secondary beam had two SWICs, both located about 1000 feet from the target. These were used in the angular divergence measurement. One SWIC had variable wire spacing<sup>7</sup> (6 mm in the center and 10 mm near the edges). The other SWIC<sup>8</sup> had 0.240 inch copper etched strips separated by 0.040 inch gaps (approximately 7 mm sampling). A differential Cerenkov counter<sup>9</sup> used in the momentum bite determination was at the same z location. Data from all these monitors as well as the currents of all the pre- and post-target magnets were recorded on magnetic tape after each spill.

MOMENTUM BITE MEASUREMENT

Figure 4 shows a layout of the Cerenkov counter used in this measurement. This counter was constructed to operate in the previous generation dichromatic neutrino beam. Because of the high instantaneous rate of secondary beam particles (about  $10^{13}$  /sec in a 1 msec fast spill), the signal output from the phototube was integrated over the spill time, thus providing a relative measure of beam particle composition. Although these tests used 20 second slow spill and utilized 100 times fewer protons on target/pulse than during previous neutrino data taking, the phototube output was still integrated over the entire spill.

Radiated Cerenkov light follows the optical path shown in Figure 4. The parabolic mirror M1 has a 305 cm focal length. Located about 5 cm beyond this focal plane is a rotatable disk, labelled 'iris', with a selection of apertures, allowing light of selected angular range to reach the phototube. Annular rings which subtended angular ranges of 0.7-1.0 mr and 1.7-2.0 mr (used in these measurements) as well as a variety of circular penetrations are available. As the pressure of the radiator is increased, the phototube sees Cerenkov light from pions, then kaons and finally protons. The Cerenkov phototube output at each pressure point is then normalized to the

secondary beam flux as measured by the ion chamber. The particle fractions are obtained from the relative area under each peak of the response curve as a function of pressure.

Also shown in the figure is a shutter which can be closed so that light produced in the main body of the counter can not reach the phototube. One then has a measure of background light produced outside the radiator, but seen by the phototube. Shutter closed points were taken at a few randomly selected pressures for each momentum. This background is measured to be independent of pressure and has been subtracted from the data to be shown.

One can approximate the Cerenkov relation as:

$$\theta_c^2 = 2KP - (m/p)^2 ,$$

where  $\theta_c$  is the angle of Cerenkov light,  $K$  is the gas constant per unit pressure,  $P$  is the pressure of the radiator (here, He gas), and  $m$  and  $p$  are the mass and momentum of the radiating particle, respectively. Because of the presence of the second term on the right hand side of the above equation, for a beam of finite momentum bite, the larger the mass of the particle, the broader the Cerenkov response. Thus, by measuring the width of the proton peak as a function of pressure, one obtains a measurement of the momentum bite of the beam.

Data were taken at secondary momenta of 200, 400, 500 and 600 GeV, in order to investigate the effects of particle production on the momentum bite. These data are shown in Figure 5. It should be emphasized that this counter was designed to operate in a lower energy range, and thus is unable to resolve pions from kaons above secondary momenta of approximately 250 GeV.

The results of the momentum bite determination<sup>10</sup> are given in Table I, along with the Monte Carlo prediction, as a function of secondary momentum. Errors quoted for the momentum bite are determined by choosing the minimum chi-squared from successive fits as the Monte Carlo input momentum bite was distorted in 2% steps from 96% to 104%. At all secondary momenta, the data are within 2% of the prediction.

It should be noted that an absolute pressure calibration (and thus an absolute momentum determination) was not available. The true pressure was obtained by scaling the measured pressure from the following formula:

$$P_{\text{true}} = (P_{\text{meas}} + (0.9 \pm 1.4)) * (0.880 \pm 0.017) \text{ torr}$$

This is the best average fit to all 4 data sets.



OTHER TESTS USING THE CERENKOV COUNTER

It was found empirically during previous neutrino running with this Cerenkov counter that small adjustments (about 5 cm) to the iris z position relative to the focal plane of the main mirror resulted in improved pion-kaon separation. The reason for this is that the small but finite secondary beam divergence makes it appear as if the beam is originating from a point source in the vicinity of the production target. By the thin lens formula, then,

$$1/f = 1/s + 1/i$$

where  $f$  is the focal length of the mirror,  $s$  is the source distance, and  $i$  is the image distance. Since the source point of this train is at a distance which is large compared to the focal length of the mirror, the sharpest image does not appear precisely at the focal plane, but slightly beyond this point.

Because only a limited amount of time was available for these measurements, the z position of the iris was not adjusted to optimize pion-kaon separation. The NCI beam has a different effective source point than the previous train, and so the iris was not located at the optimum position. Indeed, the counter had been moved several times before this measurement, so that it was decided to fit the iris location by minimizing

chi-squared to each of the fits at all secondary momenta. The final value which gave the best overall agreement was  $Z_{\text{iris}} = 303.5 \pm 0.5$  cm.

Alignment of the counter relative to the beam can also affect the width of the pion peak, and thus the pion-kaon separation. When time permitted, we did align the counter with the secondary beam by setting the pressure so that the pion light ring was slightly bigger than the iris aperture, and then adjusting both the x and y alignment of the counter to minimize the phototube output.

Since these tests were parasitic, the SWICs in the secondary beam were centered on the line pointing toward the NWest production target, about 0.5 mr off from the line pointing toward the neutrino detectors. It was decided to conduct the measurements with the secondary beam also pointed toward the NWest target, in order to avoid lengthy accesses to move the SWICs. For some of the data, not enough time was available to both align the counter and take a pressure curve, so the counter was aligned parasitically to the 800 GeV primary beam running to the NWest target, and this approximate alignment was used for the pressure curve. Subsequent checks showed that although pion-kaon separation was not optimum, the momentum bite determination was not affected.

As mentioned previously, because of the finite angular divergence of the beam, it appears to originate from a point source near the production target. Because of the specific optical design of this train, the location of the apparent source point of the horizontal plane is at a different  $z$  position from that of the vertical plane.

It has been suggested<sup>11</sup> that a third quadrupole located at the end of the train could be used to reduce the difference in the  $z$  positions of these apparent source points, and thus give an improved pion-kaon separation. Monte Carlo calculation showed this to be true, giving about a 17% improvement in the effective beam divergence as seen by the Cerenkov counter, with only a 2% degradation in the energy resolution of the neutrino beam at the detectors (see Figure 6).

Measurements taken with this quad at the theoretical value were indistinguishable from those taken with the quad off. The finite length of the counter (which causes diffraction broadening<sup>9</sup>), non-optimized iris position and approximate alignment could all have contributed to a null result. This measurement should be re-done with the new Cerenkov counter<sup>12</sup> before data taking begins.

Particle fractions determined from these data are given in Table II, along with predictions from a particle production model<sup>13</sup>. Only the proton fractions and, at lower momenta, the pion fractions should be taken seriously. Even so, the agreement with prediction is remarkable.

### ANGULAR DIVERGENCE MEASUREMENT

Figure 7 illustrates why it is important to have small angular divergence in a dichromatic beam. For low secondary momenta, the divergence of the beam is a small contributor to the neutrino energy resolution at the detectors compared to the momentum bite of the beam. For momenta in excess of 400 GeV or so, the beam divergence plays an increasingly important part in this energy resolution. In fact, for 600 GeV secondaries, a 0.2 mr divergence produces an unacceptably large resolution at large detector radii, even for a beam with no momentum spread. In addition, if one uses a Cerenkov counter to determine particle fractions in the beam for a flux determination, small angular divergence is crucial for pion-kaon separation.

As part of the initial set of tests of the new dichromatic train, it was thus appropriate to measure the angular divergence of the beam. The technique used is graphically shown in Figure 8. A (16 inch x 16 inch) 10 foot long steel

collimator<sup>14</sup> with a 1/2 inch square hole running down its axis was placed in the path of the secondary beam just before the final set of bending magnets. The collimator was aligned parallel to the trajectory of the central ray. The size of the beam at this point was approximately 6 inches high by 3 inches wide, primarily determined by upstream magnet apertures. This collimator (called the Hole Collimator) was swept across the beam horizontally in 1/4 inch steps and vertically in 1/2 inch steps, sampling small segments of the beam phase space at each position. (Originally it was also planned to utilize 1/4 inch steps vertically, but time did not permit this fine a grid search.)

Located about 825 feet downstream from the Hole Collimator in the Expansion Port were two SWICs, where beam profiles from each individual grid point were recorded, along with primary and secondary beam intensities. Because of inherent design features in the SWIC readout system, 5 scans in time were taken across the spill. Figure 9 shows these scans for one of the SWICS on a collimator out spill. Scans 2-4 were subsequently combined for this analysis. Because the distance between the Hole Collimator and the SWICs was so large, one can effectively think of each grid point as a point source of particles, and thus the spatial distributions measured by the SWICS can be transformed into horizontal and vertical angular distributions of rays from each sampled region of the beam. The individual

angular distributions, weighted by the intensity in the secondary beam for each point, can then be combined to give a measure of the total angular divergence of the beam. This technique has been used in the past<sup>15</sup> to measure the angular divergence of a previous dichromatic beam.

Several problems complicated this measurement:

1. Monte Carlo study has shown that the angular divergence of the secondary beam is a strong function of the proton beam spot size on target. Figure 10 shows that this effect is much stronger for a large horizontal extent of the beam than it is for a large vertical extent. Indeed, for horizontal beam sizes above 1 mm (half width at the base), the divergence rises linearly with beam size. Unfortunately for these measurements, the pre-target optics were constrained by the slow spill test beam program, and the spot size on target was limited to approximately 3 mm H x 1.5 mm V, (see Figure 11). Subsequent to taking this data, the switchyard optics have been re-done. With this new optics, a horizontal spot size of less than 1 mm can be achieved. Because of this inherent problem, final results for the angular divergence of the beam can not be stated, as they are so strongly coupled to the horizontal beam spot size. Instead results will be presented comparing the data to a Monte Carlo which also had a comparable proton beam spot size.

2. As had been mentioned previously, these data were taken with the secondary beam pointed toward the NWest production target. The bend needed to steer the beam this direction introduced an additional small angular divergence to the beam. This effect was included in the Monte Carlo calculations for purposes of comparison.

3. Because of the large mass of the Hole Collimator, several support mechanisms were attempted before one was found which allowed the collimator to retain the same spatial alignment over its entire field of travel. The final modification was made in situ, and was such that the bottom 1/2 inch of the beam phase space could not be measured. This will be corrected for future studies. In addition, the final support system was installed near the end of the run, when accelerator failures were increasing due to lead problems in the super-conducting magnets. These time constraints, along with proton economic constraints, limited data taking to one 8-hour scan.

4. It was discovered prior to the Hole Collimator scan that the stepping motor control circuitry for positioning the collimator was strongly temperature dependent, and thus led to a day-night difference in actual movement for a fixed number of input steps (see Figure 12). Since it was important to sample the beam phase space uniformly, a C-BASIC program was written which operated on the EPICS control system and used the position read-back to correct for this temperature dependence.

This technique worked extremely well. For future studies, however, the control electronics should be modified to correct this complication.

5. Probably the most serious problem encountered which compromises analysis of these data is the lack of redundancy in beam monitors. Part way through the scan, electronics associated with the ion chamber (the secondary beam intensity monitor) failed in such a way that the outputs for both the signal and for an off-spill pedestal varied by several times the typical signal level (see Figure 13). Since these fluctuations were so large, only approximate point to point normalization is possible. This anomaly is evident in about 1/3 of the data taken. At the time, the variation in beam intensity was attributed to mis-steering of the primary beam, as no other monitors were available for cross-check. Time ran out before the affected part of the scan could be repeated once the electronics had again stabilized. In addition, the 6 mm SWIC located in the Expansion Port did not give reliable profiles (many missing wires) at the low intensities encountered during the scan. Thus, this analysis is done solely with the 7 mm strip SWIC.

6. Proton economics also contributed to the complexity of this analysis. Initial calculations showed that about  $5 \times 10^{12}$  protons per pulse were the minimum needed for the scan. Most of the data were taken at about  $2 \times 10^{12}$  protons per pulse.



Figure 14 shows the signal to noise inherent in the data for a point near the edge of the beam phase space, where the intensity is quite low relative to the center of the beam. More protons would have enhanced the signal to noise, however, low intensity points such as this one may never be analyzable. It should be noted that in addition to a beam-off pedestal pattern made by averaging over all beam-off pulses in the course of the scan, a flat background was subtracted from each SWIC display before comparing the data to Monte Carlo prediction. For asymmetric profiles, this will introduce a bias in the tails of the distributions. Probably more sophisticated background methods can also be developed in future, utilizing a different background level for each side of the peak.

7. The Hole Collimator was not located at the end of the train where the beam is most parallel, in order to utilize the B-d1 provided by the final set of dipoles to sweep away any off-momentum particles created by scraping in the collimator. At this intermediate location, the beam still has some divergence, so that not all of the particles which enter the upstream of the collimator aperture are transmitted through to the end. Unless one is able to use a grid whose steps are smaller than the hole size, one obtains an under-estimate of the beam divergence. Time constraints did not permit 1/4 inch sampling in the vertical direction. To compensate for this,

the Monte Carlo calculations included a cut on the positions of the rays at the downstream end of the collimator in order to simulate this effect. In future, more points can be taken, or a shorter collimator (of Tungsten) can be used.

For purposes of presentation, the data were divided into 9 roughly equally populated regions in x and y. Figure 15 shows this division. A representative individual point from each of the 9 regions is shown in Figure 16 (a-i), along with the Monte Carlo predictions for a 1 mm and a 3 mm horizontal proton beam spot size on target. As can clearly be seen in the figures, the 3 mm spot more closely approximates the data. Also evident is the increase in the beam divergence, in both the horizontal and vertical planes, for the larger spot size.

Because of the problems inherent in background subtraction, a measure of the width of each curve should provide a more meaningful comparison between the data and the Monte Carlo prediction than the tails of these distributions. For each grid point, both the data and the corresponding Monte Carlo distributions were fit with a gaussian. The ratio of the sigmas of these two fits provided the figure of comparison.

Table III shows this ratio averaged over each of the nine regions for both the vertical and horizontal planes. The data and the prediction are seen to agree within about 10% for the horizontal plane, and within about 35% for the vertical plane, with the horizontal plane data being slightly smaller than the prediction, and the vertical plane data being larger than the prediction. Figure 17 shows a sum over all 9 regions of these ratios, both unweighted, and with each grid point weighted by its intensity as seen by the ion chamber.

It is possible that a quadrupole had been incorrectly set during the scan. A subsequent study of the magnetic field in one of the 4-Q-120 quadrupoles from the train showed that the B vs I response of the quad was within 2% of the theoretical value. It was discovered, however, that the transducer used to measure the current in the quad had a non-linear response for small currents compared to a precision shunt which gave a linear response with input setting (see Figure 18). An incorrect current in this quadrupole of up to 10% can not be ruled out. Indeed, a Monte Carlo run with a 3 mm horizontal spot and 7.5% less current than design gave slightly better agreement with the data (see Figure 19). The readouts for all power supplies on the train will be modified for the next run to better measure the actual current.

SUMMARY

The initial tests of the NCI dichromatic train showed that the momentum bite was within 2% of design. Though the data is by no means definitive, the particle fractions measured at 800 GeV are reasonably close to those predicted from 400 GeV data. A first look at the angular divergence of the beam showed it to be within 10% of design in the horizontal plane and about 35% greater than design in the vertical plane. Several problems were discovered which will be corrected before the next run.

## References

1. L. Stutte, "Further Design Studies for a Tevatron Era Dichromatic Beam", Fermilab technical memo TM-1091, 1982.
2. Magnet inserts NC1W-1,2, Fermilab drawings 2920-ME-162416,7.
3. Beam dump assembly, Fermilab drawing 2910.100-ME-162243.
4. Participants in these measurements were D. Owen, Michigan State University, and S. Pordes, P. Rapidis and L. Stutte, Fermilab.
5. Secondary Emission Monitor, made by L. N. D. Inc., 3230 Lawson Blvd., Ocean Side, New York, 11572.
6. R. Blair, et al, "Monitoring and Calibration System for Neutrino Flux Measurement in a High-Energy Dichromatic Beam", Nucl. Instr. and Meth. Phys. Res. Sect. 226, 281 (1984).
7. Expansion Port SWIC, Fermilab drawings 2963-ME-108706,7.
8. Expansion Port strip SWIC, Fermilab drawing 2932-MD-162134.
9. A. Bodek, et al, "Observation of Light Below Cerenkov Threshold in a Short Cerenkov Counter", Zeit. fur Phys. C, 18, 289, (1983).
10. The analysis of the Cerenkov data was carried out by J. Marko, MIT.
11. F. Sciulli, private communication.
12. F. Borcharding, "A Cerenkov Counter Design for a High Energy, High Intensity, Secondary Beam", Fermilab technical memo, in preparation, March 1986.
13. A. J. Malensek, "Empirical Formula for Thick Target Production", Fermilab note FN-341, 1981.
14. Hole Collimator, Fermilab drawing 9208.050-ME-201032.
15. C. Haber, "A Search for the Inclusive Oscillations of Muon Neutrinos", Ph.D. Thesis, Columbia University, 1985.

TABLE I.

## Momentum Bite Measurement

Train Momentum	Measured Momentum Bite	Predicted Value
GeV	%	%
200	14.1 +/- 0.3	13.8
400	11.1 +/- 0.3	11.4
500	10.4 +/- 0.3	10.2
600	8.9 +/- 0.3	8.7

TABLE II.

## Particle Fractions (pion:kaon:proton)

Train Momentum	Measured Fractions	Predicted Values
GeV	%	%
200	58.6 : 5.7 : 35.7	57.9 : 6.6 : 35.5
400	20.2 : 1.6 : 78.5	19.5 : 3.1 : 77.4
500	7.8 : 1.0 : 91.2	8.1 : 1.6 : 90.4
600	2.1 : 0.6 : 97.2	2.8 : 0.7 : 96.4

TABLE III.

Comparison of Data/ 3 mm Monte Carlo  
for the Angular Divergence of the Beam

## VERTICAL

	EAST	CENTER	WEST
TOP	1.30	1.34	0.80
CENTER	1.43	1.53	1.28
BOTTOM	1.31	1.43	1.13

## HORIZONTAL

	EAST	CENTER	WEST
TOP	1.27	1.11	1.09
CENTER	1.03	1.09	0.81
BOTTOM	0.99	0.99	0.80

## Figure Captions

Figure 1: Neutrino event rates (cc + nc) per hundred tons per  $10^{13}$  protons in a detector of 1.35 m radius located at Lab C. Rates are shown for pion and kaon (+/-) parents as a function of parent momentum for 1 TeV on target.

Figure 2: Layout of the NCI dichromatic train, vertical and horizontal projections. The third quad located at the end of the train, used in some of the Cerenkov counter tests, is not shown.

Figure 3: Layout of the Neutrino area from NW1 to the end of the decay pipe, showing the location of the NCI dichromatic train and various monitors used in the test.

Figure 4: Schematic of the Cerenkov counter used in the tests.

Figure 5: Various pressure curves taken during the tests, for 200, 400, 500 and 600 GeV secondaries. The 200 and 400 GeV curves were taken with the 2 mr iris, while the 500 and 600 GeV curves used the 1 mr iris.

Figure 6: Effects on the actual secondary beam divergence and the effective divergence as seen by a Cerenkov counter placed at two different z locations, as a function of field in a third quadrupole located at the end of the train.

Figure 7: Energy resolution versus radius at the detectors of neutrinos from kaon decay as a function of secondary beam divergence and momentum bite, for secondary momenta of 400 and 600 GeV.

Figure 8: Schematic of the Hole Collimator measurement, showing the 10 foot collimator with the 1/2 inch square aperture used to select small segments of the beam phase space, the ion chamber used to measure secondary beam intensity, and the strip SWIC located at the Expansion Port where beam profiles were accumulated as a function of collimator position.

Figure 9: Five separate SWIC scans during one accelerator spill from the strip SWIC, showing the entire beam profile. (Hole Collimator out data ).

Figure 10: Secondary beam divergence as a function of spot size on target shown separately for increasing horizontal (H) and vertical (V) size.

Figure 11: Proton beam spot size on target for these tests, as



recorded by a  $1/4$  mm SWIC located 0.5 feet in front of the target. Note the 2 hot wires on the vertical display and the missing wires in both the horizontal and vertical displays.

Figure 12: Variation in the Hole Collimator motion for a fixed step size as a function of time, showing the temperature dependence of the positioning electronics.

Figure 13: Variation of the pedestal signal from the ion chamber as a function of time. Plotted for reference is the Hole Collimator horizontal position, indicating about 4 of the 12 scans were affected.

Figure 14: Vertical and horizontal SWIC pictures and the corresponding Monte Carlo predictions for a low intensity point during the Hole Collimator scan.

Figure 15: The division of grid points taken during the Hole Collimator scan into 9 aggregate regions.

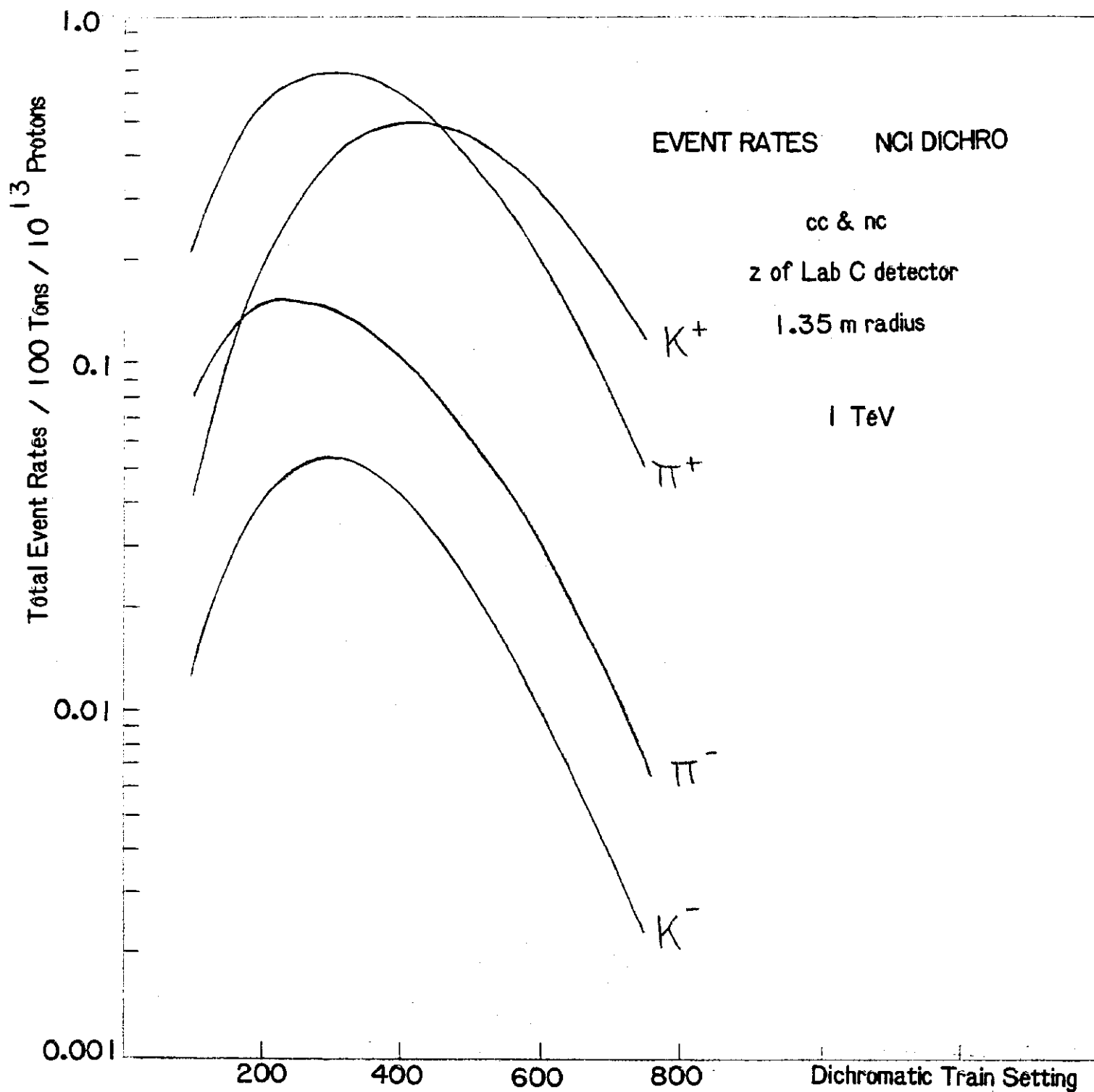
Figure 16 (a-i): Vertical and horizontal SWIC pictures selected at random from each of the nine regions. Also included are Monte Carlo predictions for the corresponding Hole Collimator positions, showing separately the predictions for a 1 mm horizontal and a 3 mm horizontal proton beam spot size on target. Note the hot wires at the right side of some of the vertical traces. This affected about  $2/3$  of the data, and was subtracted for the analysis.

Figure 17: Histograms of the ratios of sigmas of fits to data divided by sigmas of fits to the 3 mm Monte Carlo cut to simulate the same Hole Collimator position, summed over all collimator positions, for vertical and horizontal data, separately. Data are entered unweighted (left graphs) or weighted by the secondary beam intensity observed for each point (right graphs).

Figure 18: Nonlinearity in the current readout as a function of current for one of the train quadrupoles.

Figure 19: Ratios of sigmas of fits to data / fits to a 3 mm Monte Carlo which also has one of the train quadrupoles set to 7.5% less current than design: vertical and horizontal, unweighted and weighted by beam intensity. The high tail on the vertical histograms arises mainly from the bottom sections of the scan.

Figure 1.



NCI TRAIN  
750 GEV

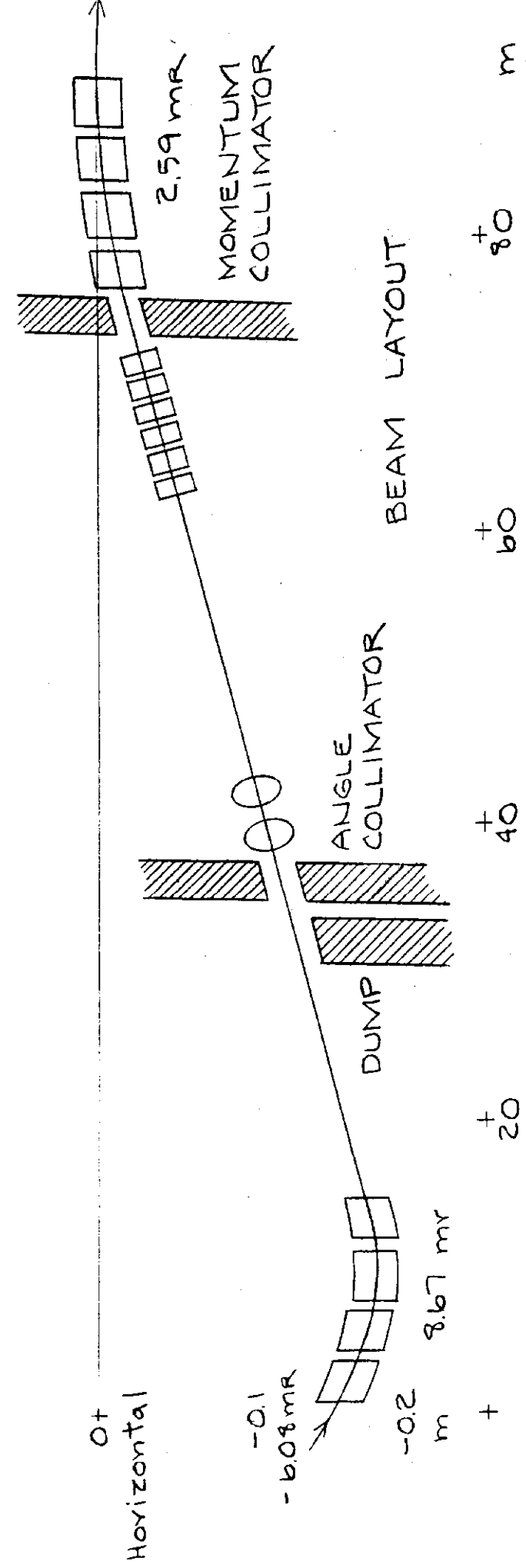
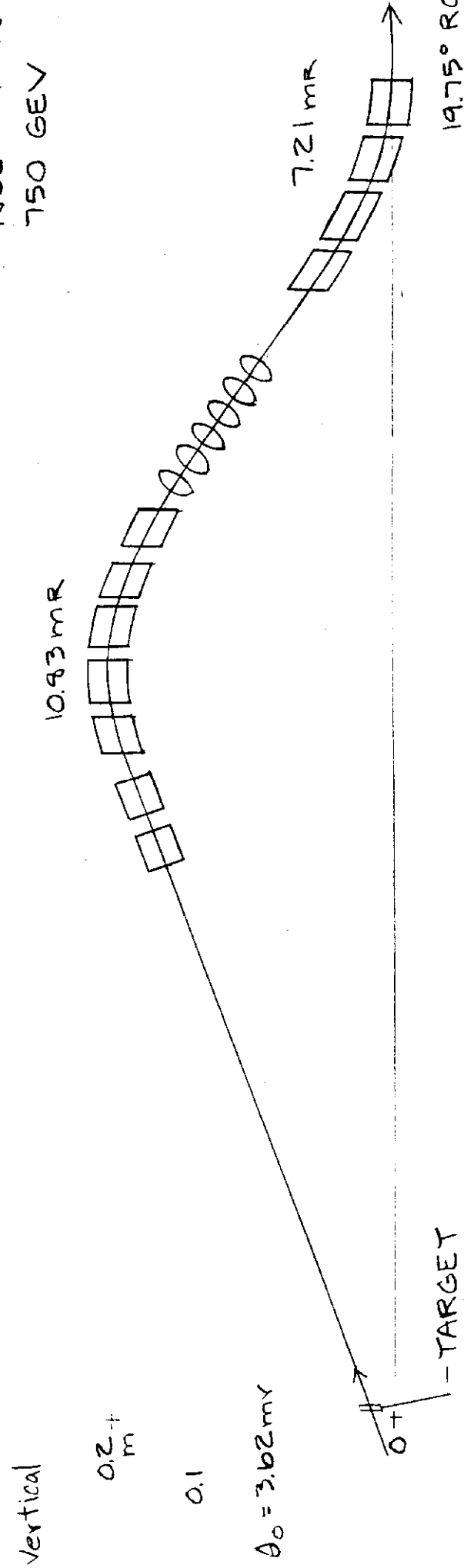


Figure 2.

## LOCATION OF MONITORS

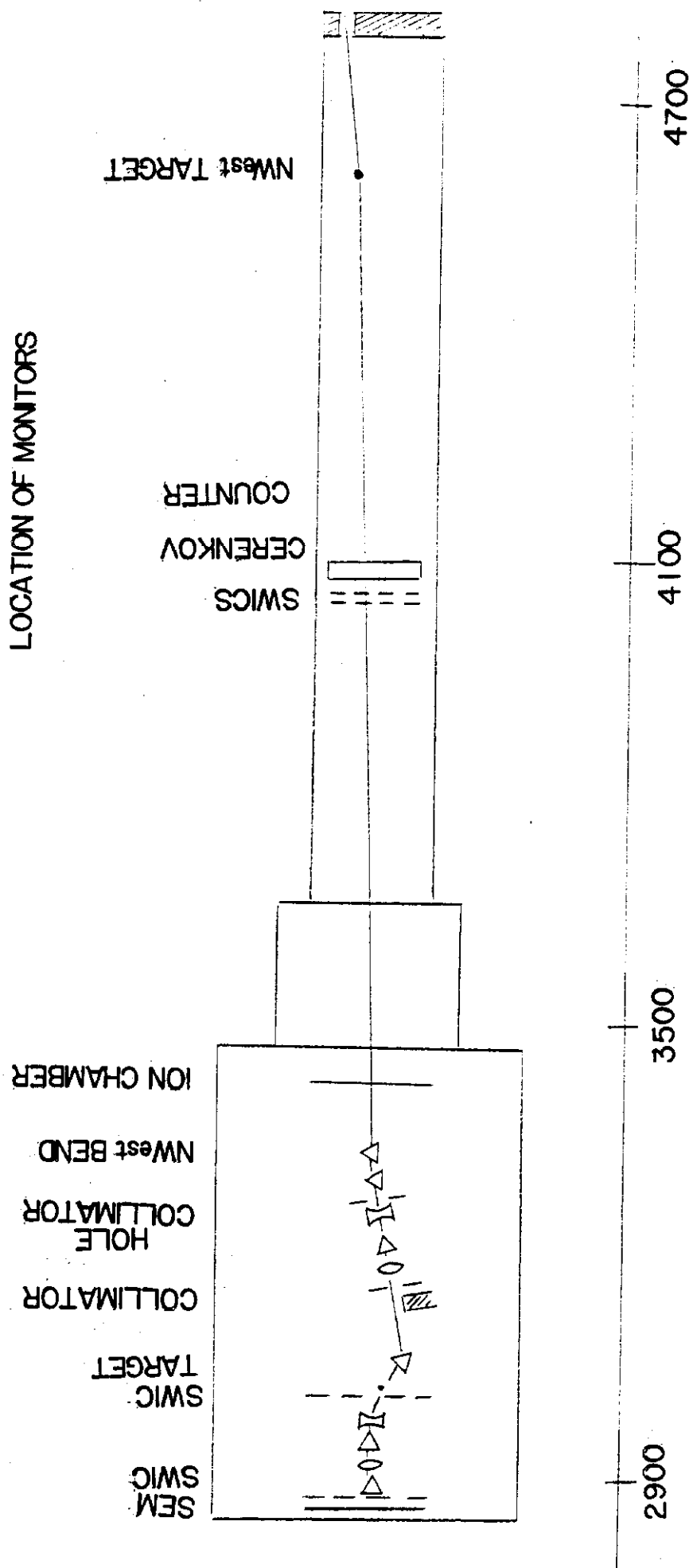
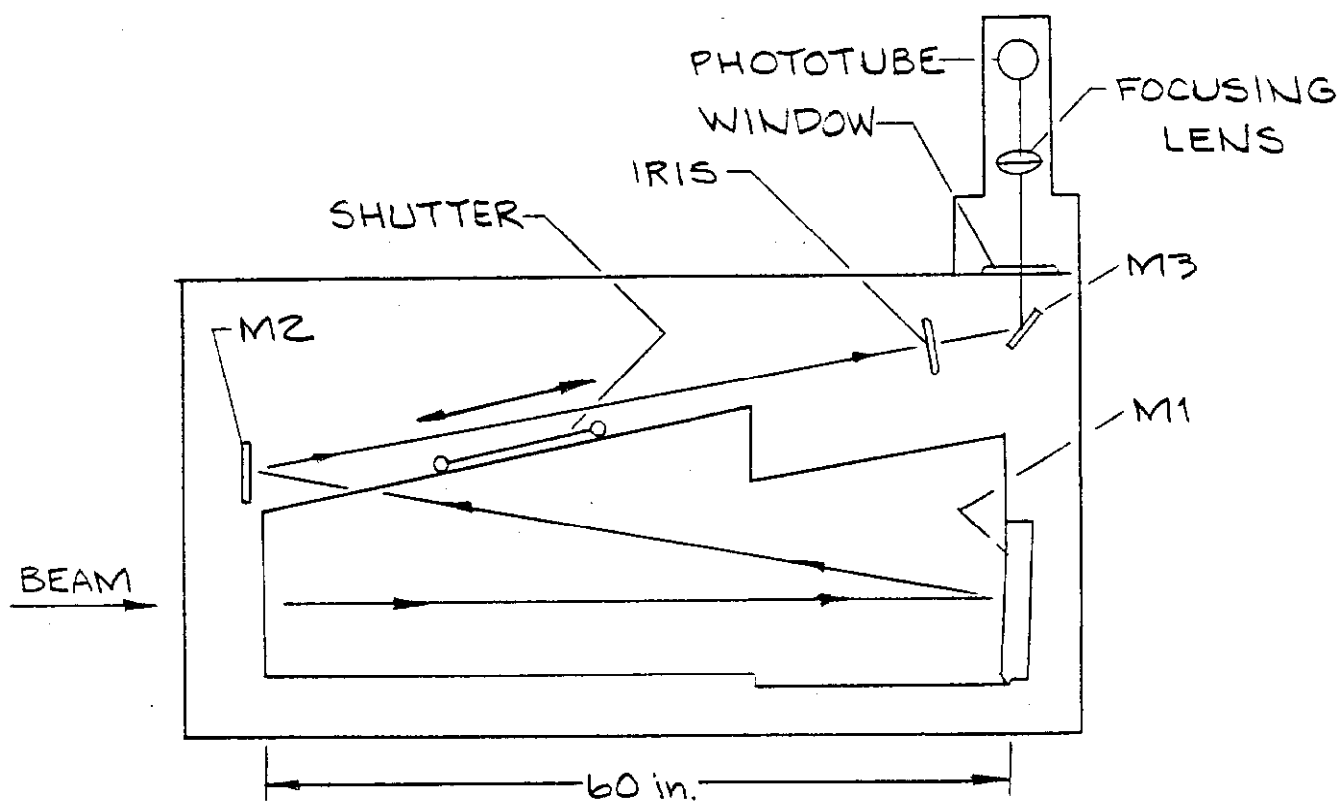


Figure 3.

feet

Figure 4.



CERENKOV COUNTER USED IN THE TESTS

## PRESSURE CURVES TAKEN DURING THE TESTS

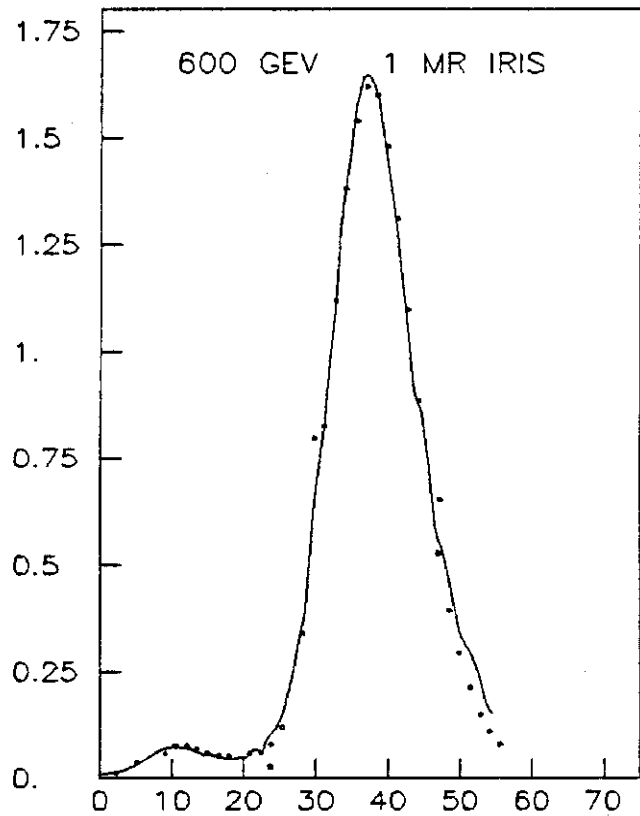
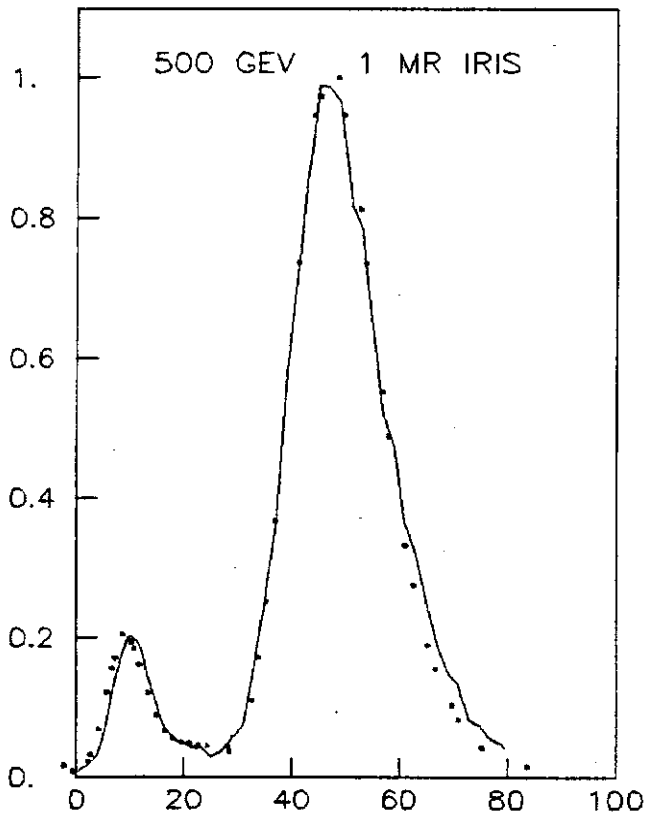
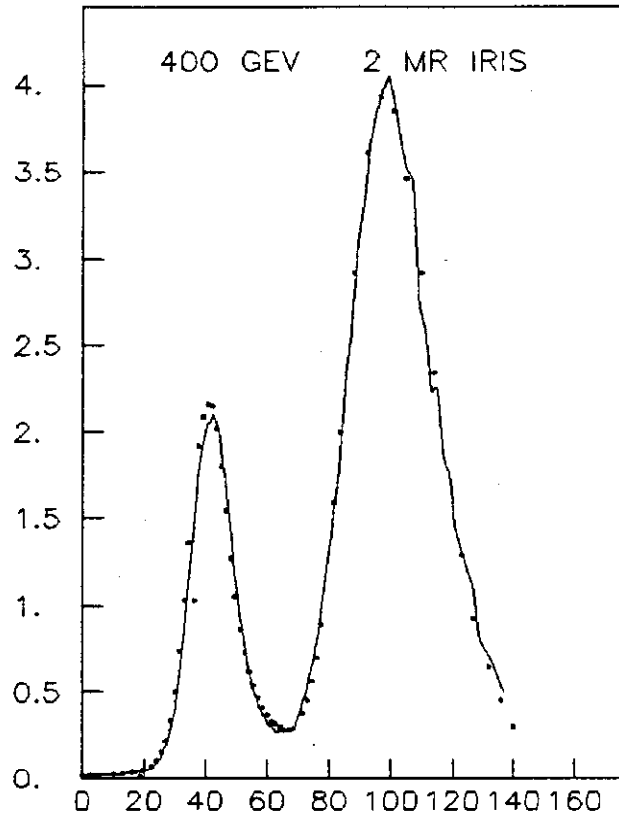
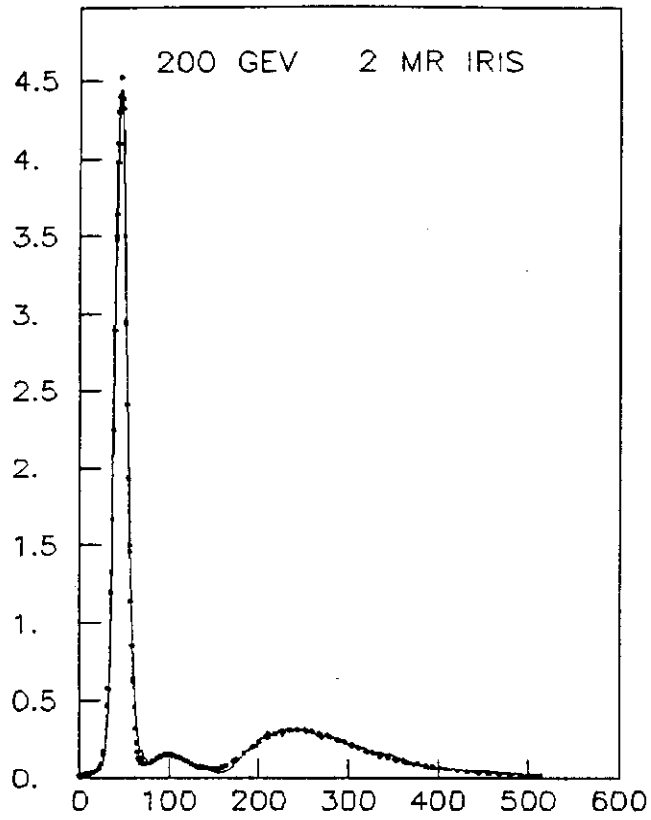
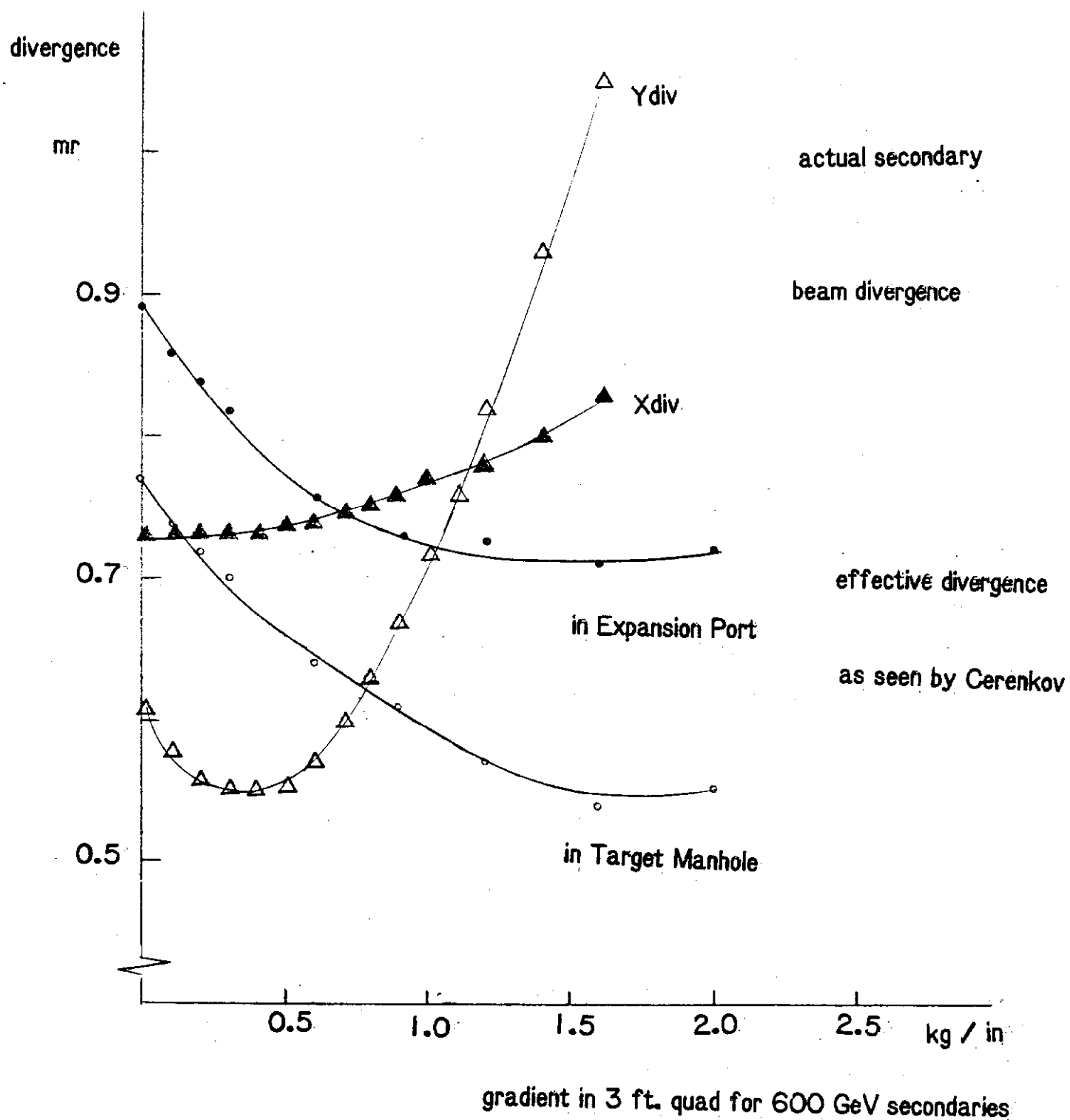


Figure 6.

## ADDITION OF A THIRD QUAD AT THE END OF THE TRAIN



# ENERGY RESOLUTION OF NEUTRINOS FROM Kμ2 AS A FUNCTION OF DIVERGENCE AND MOMENTUM BITE

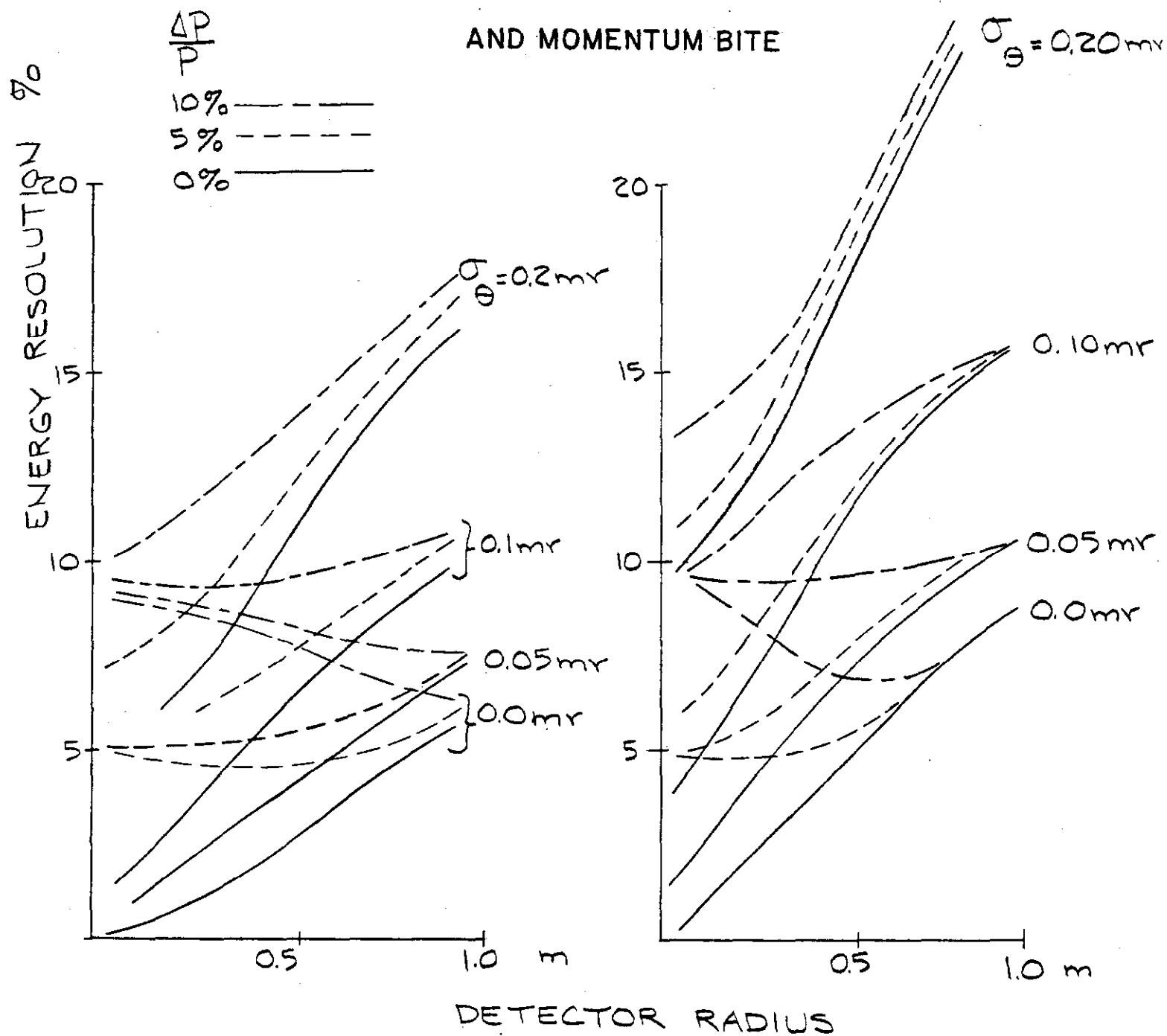
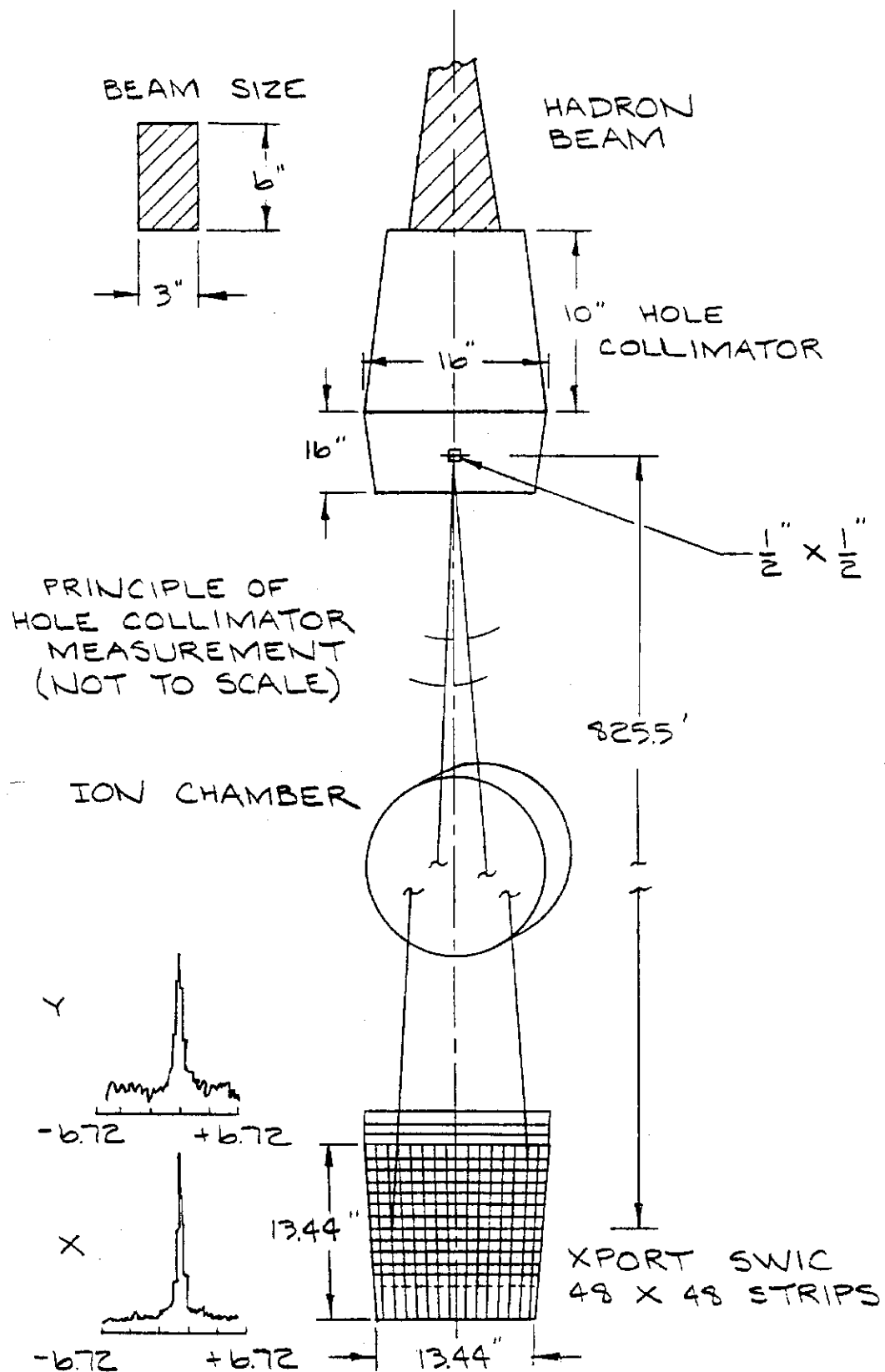
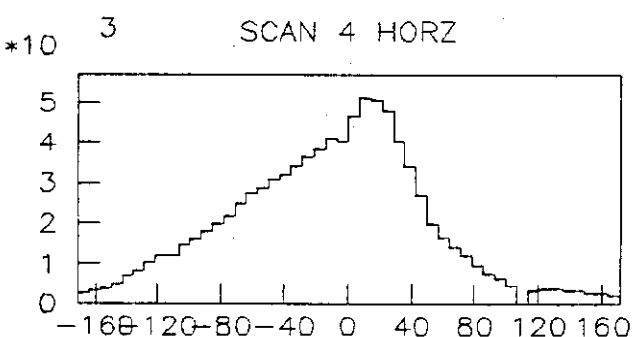
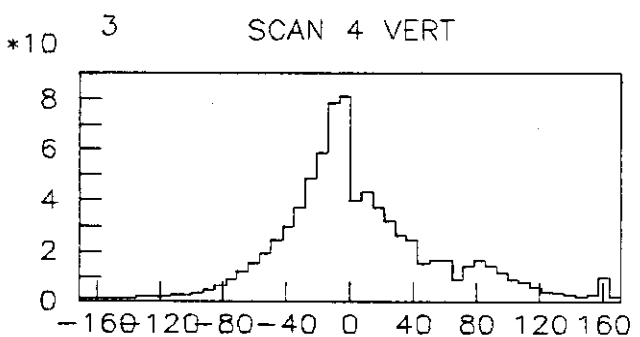
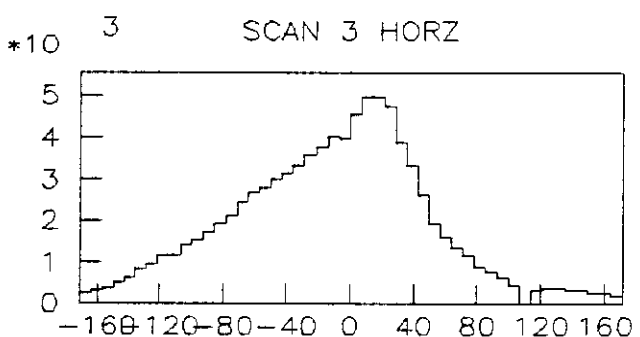
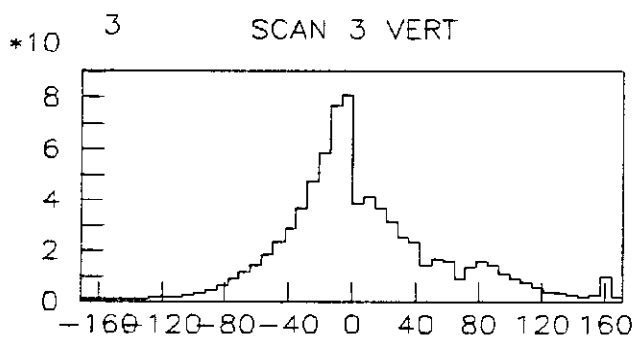
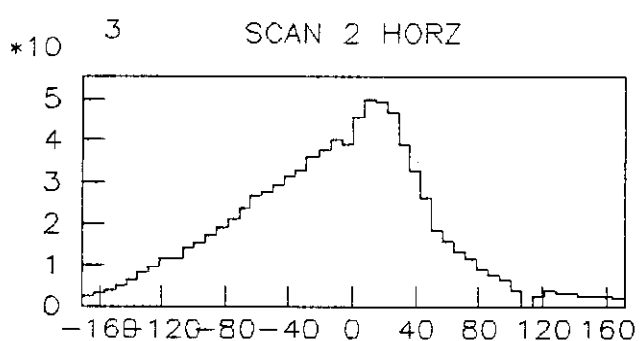
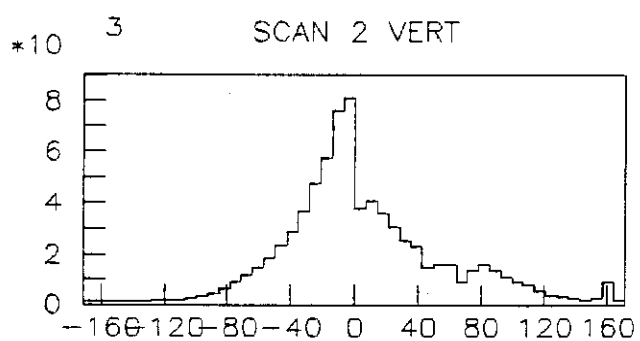
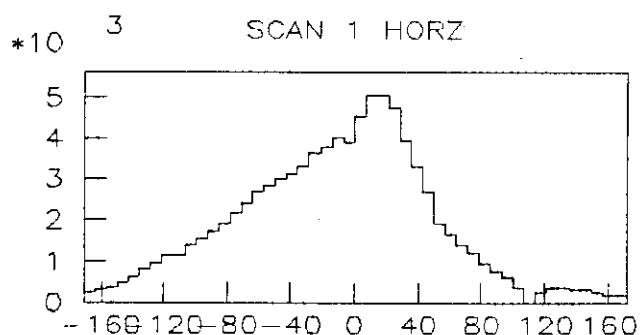
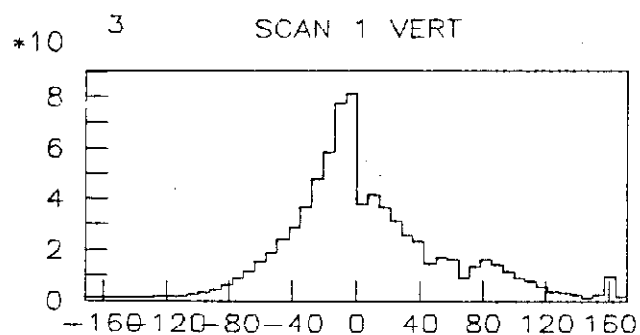
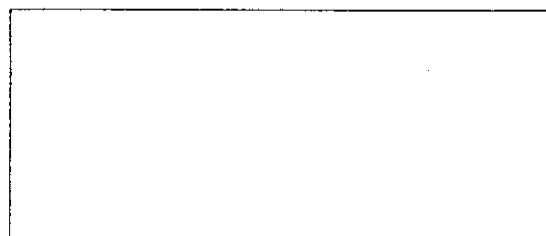
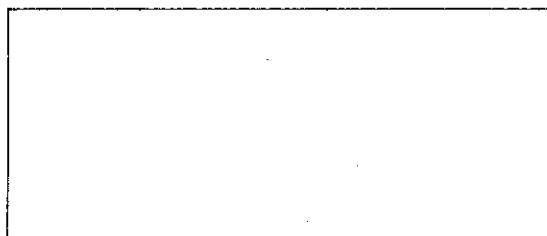




Figure 8.



## EXPANSION PORT SWIC-1 7.11 MM



SCAN 5 VERT

SCAN 5 HORZ

EFFECT OF SPOT SIZE ON TARGET  
ON SECONDARY BEAM DIVERGENCE

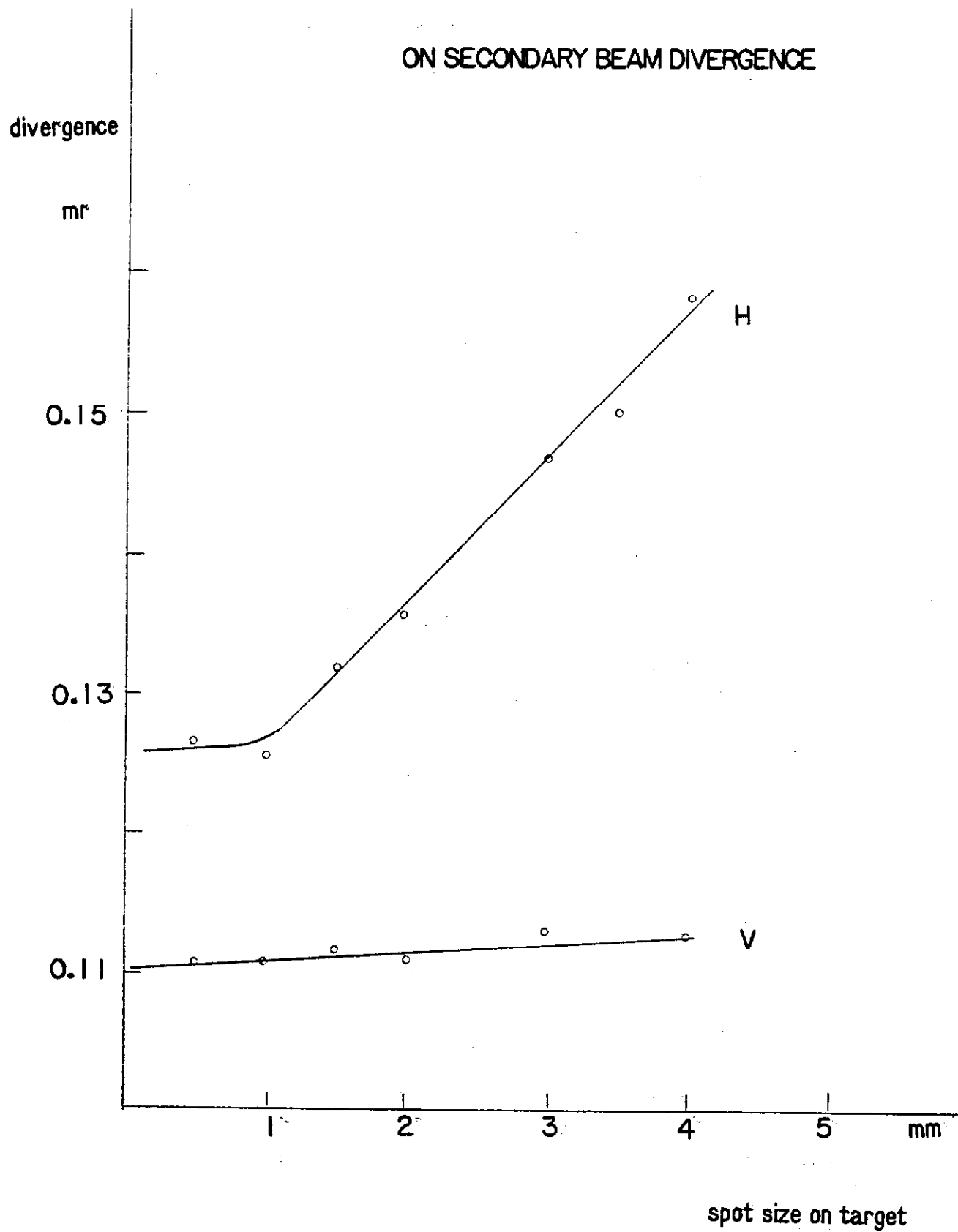
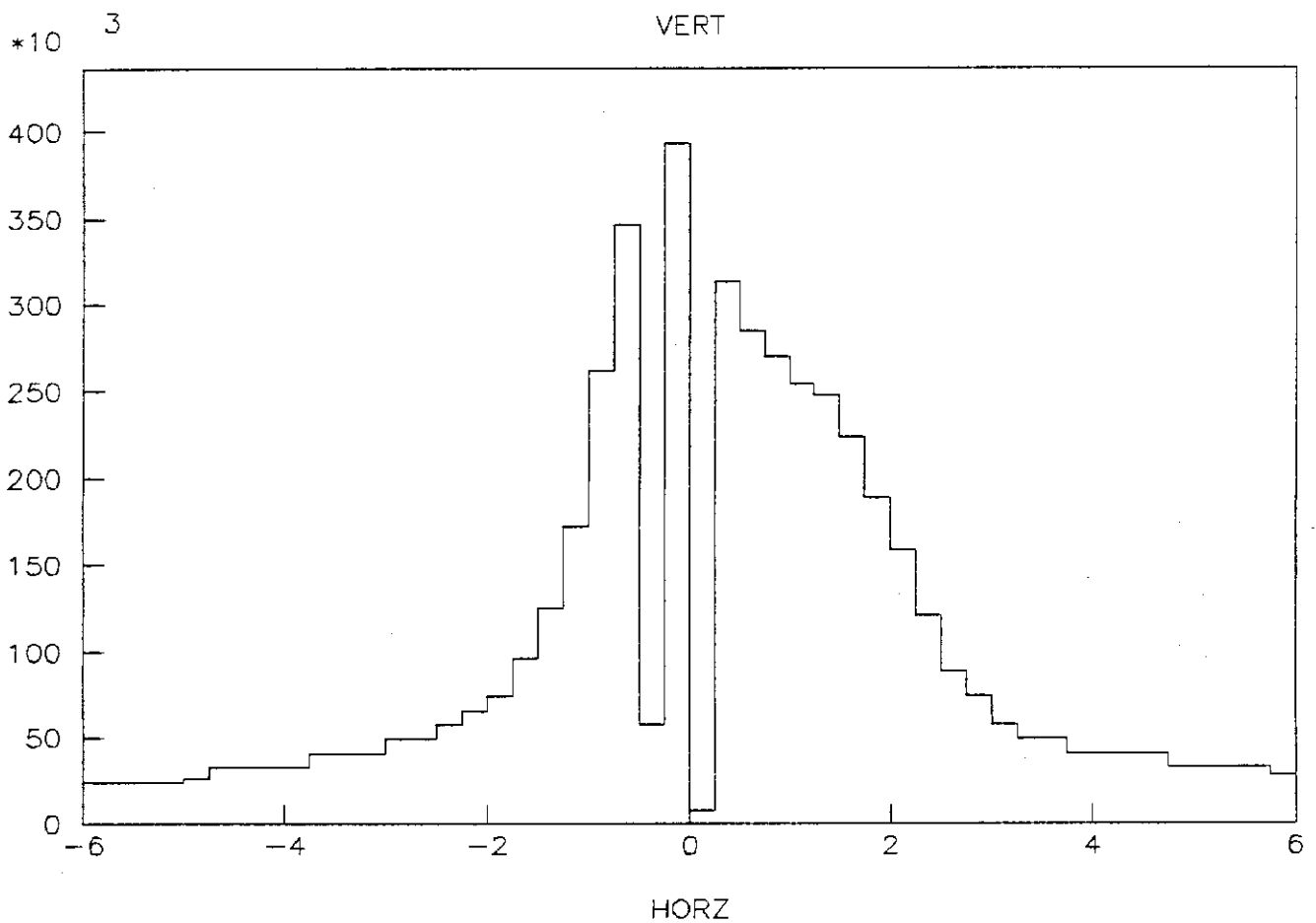
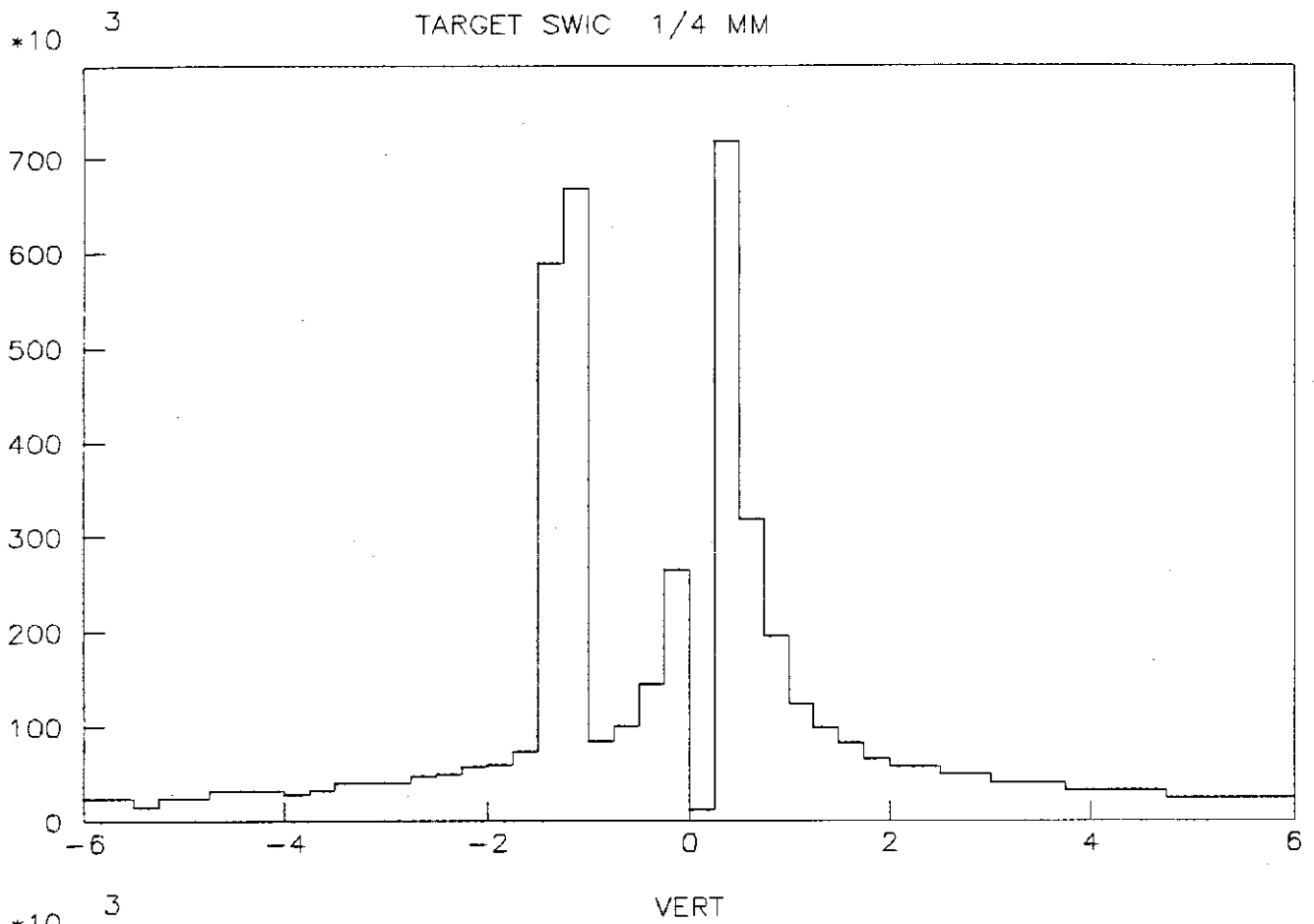
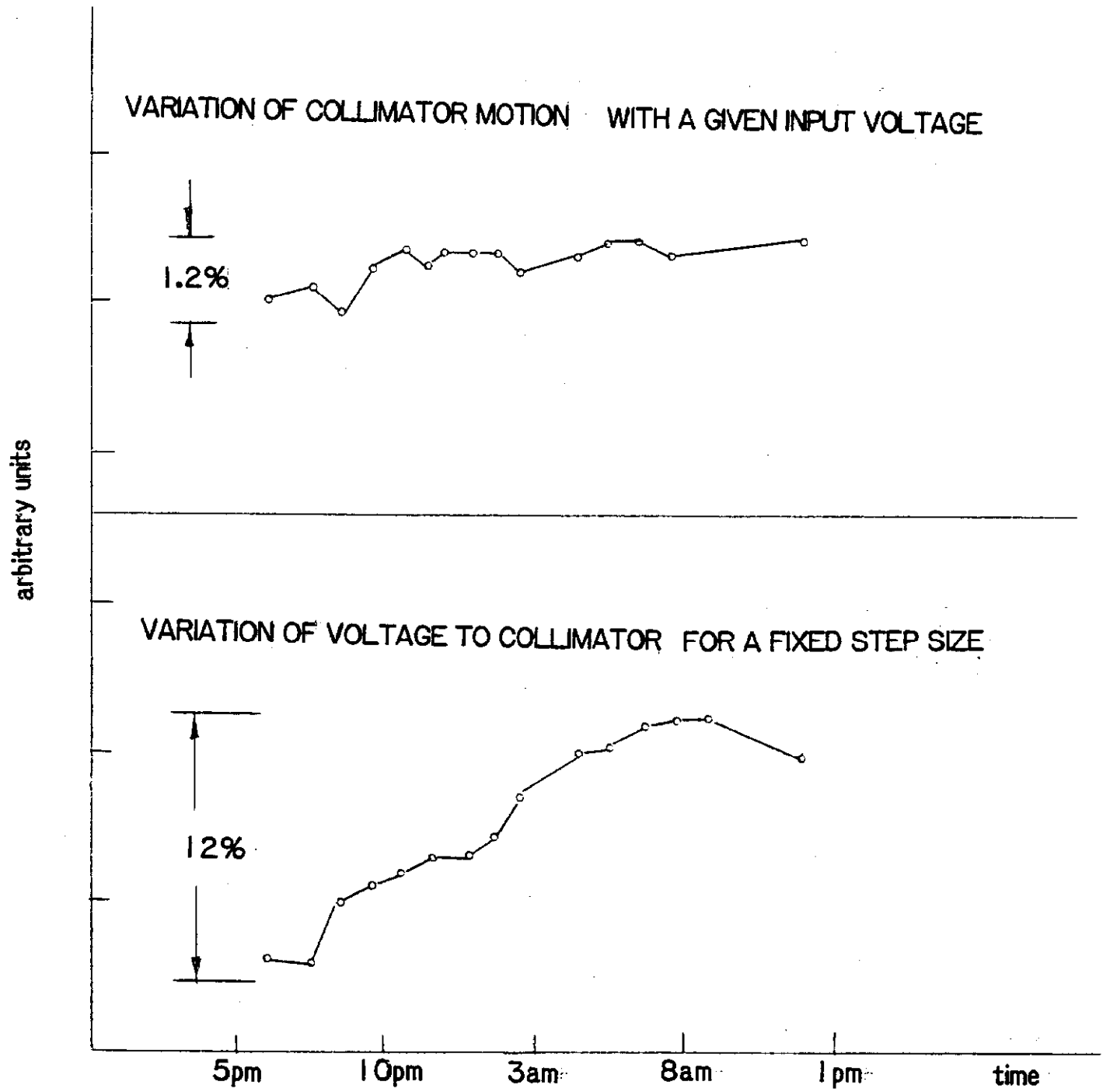
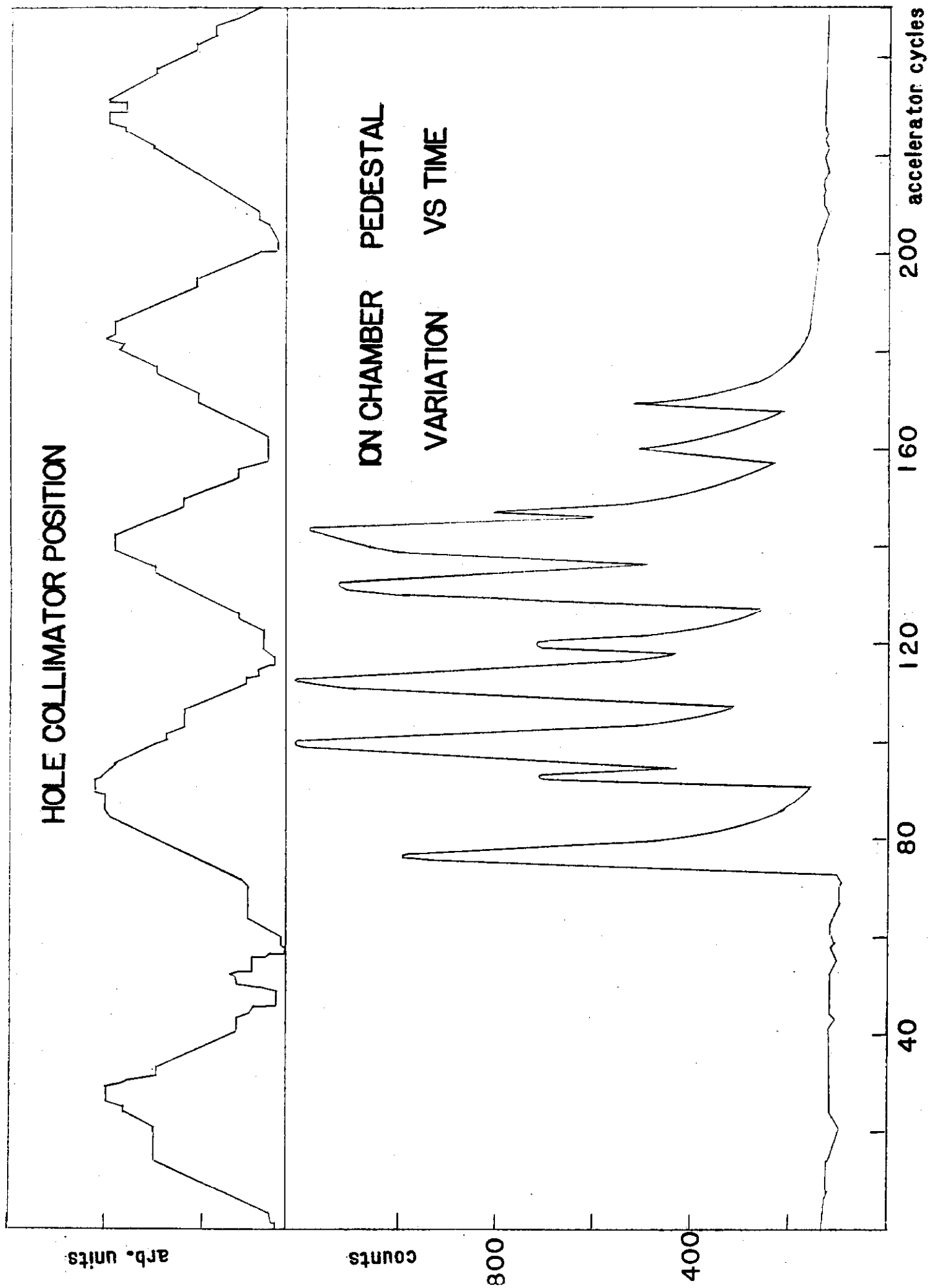


Figure 11.

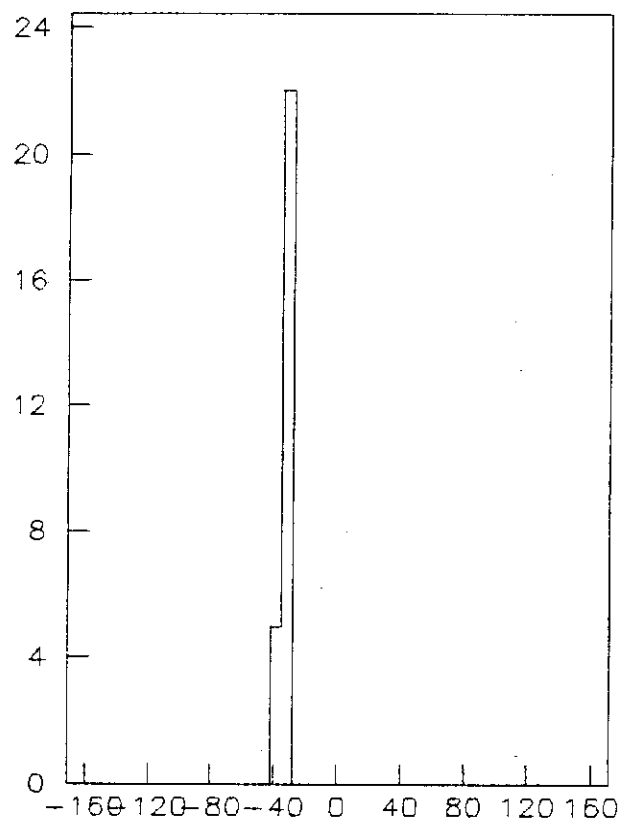


## DIURNAL VARIATION OF HOLE COLLIMATOR MOTION FOR A FIXED STEP SIZE

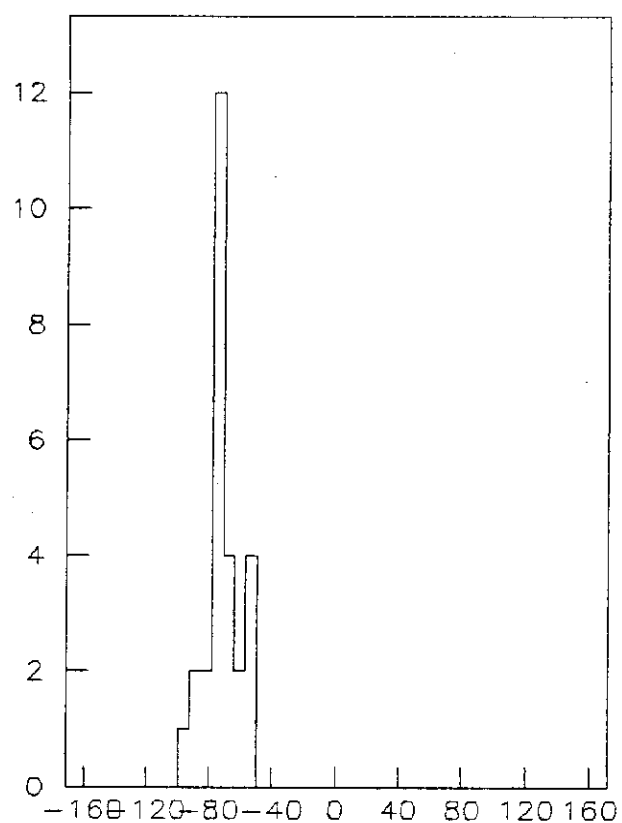




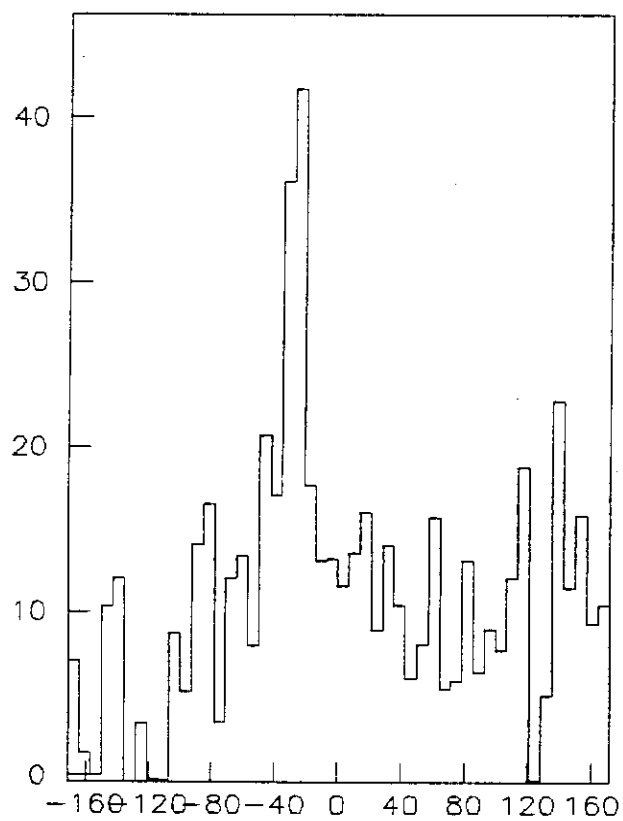
## LOW FLUX POINT



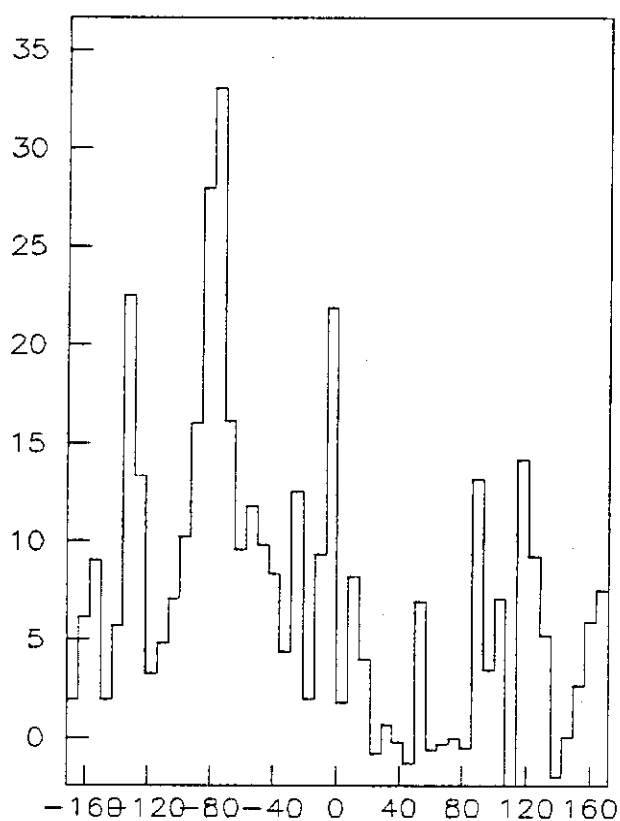
VERT 3 MM HORZ SPOT



HORZ 3 MM HORZ SPOT



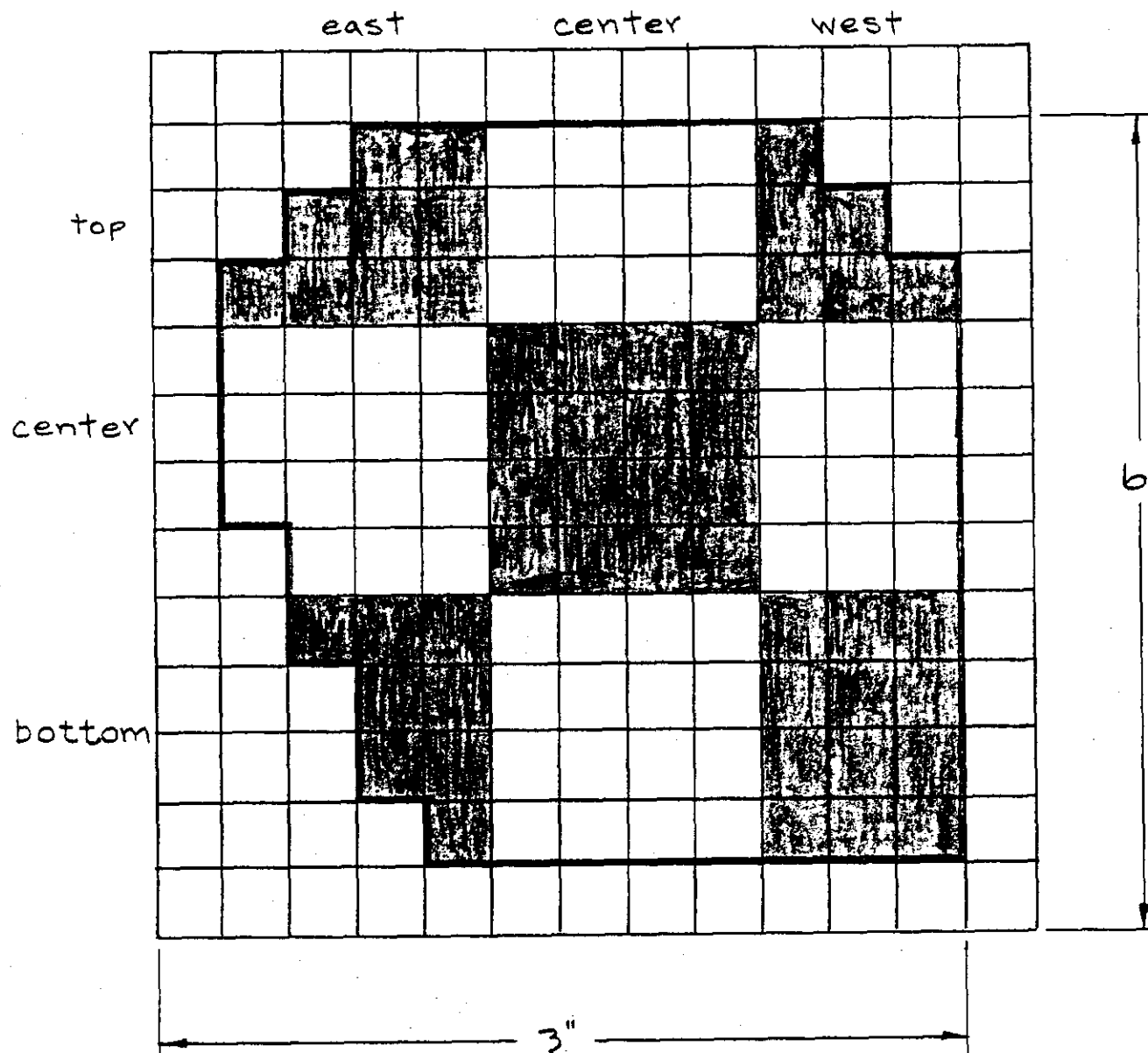
VERT DATA



HORZ DATA

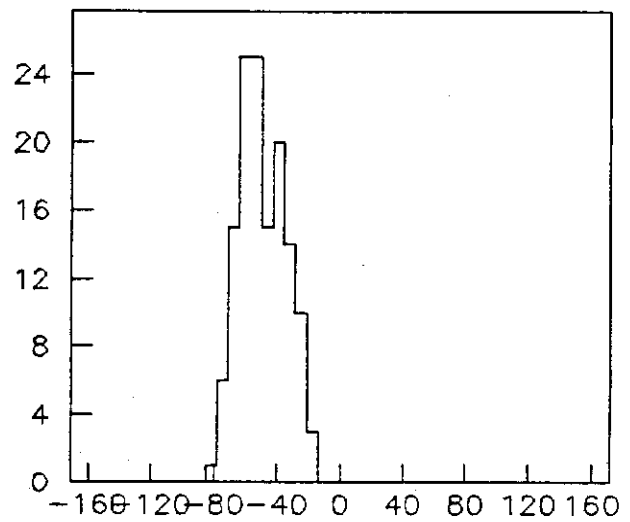
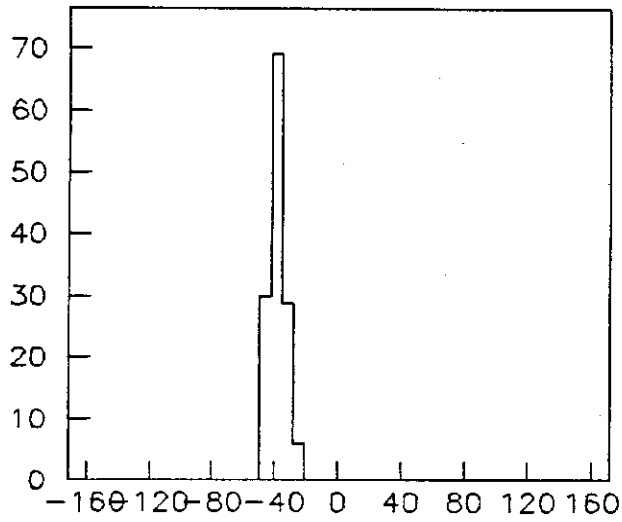
Figure 15.

# DIVISION OF HOLE COLLIMATOR POINTS

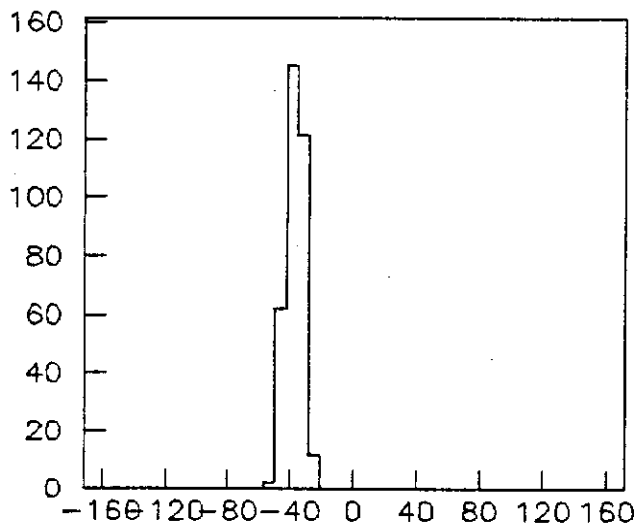




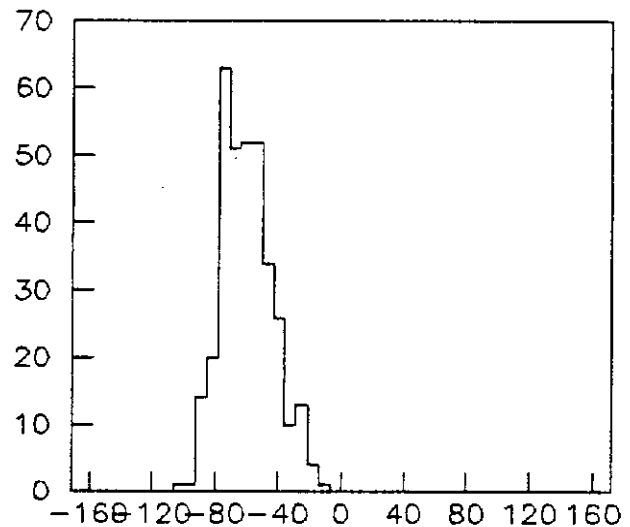
## BOTTOM EAST SECTION



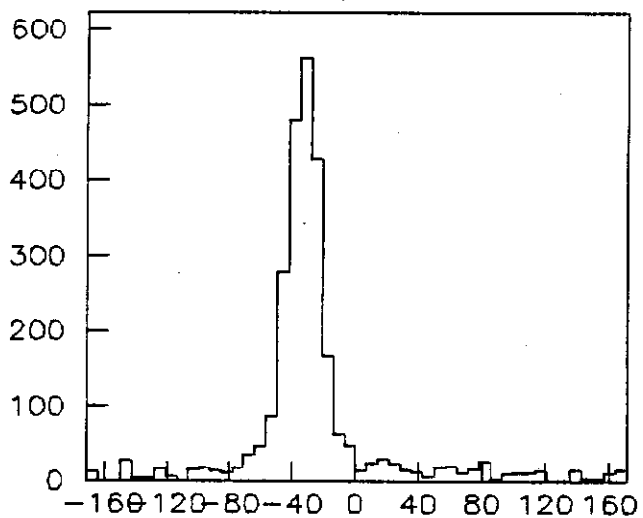
## VERT 1 MM HORZ SPOT



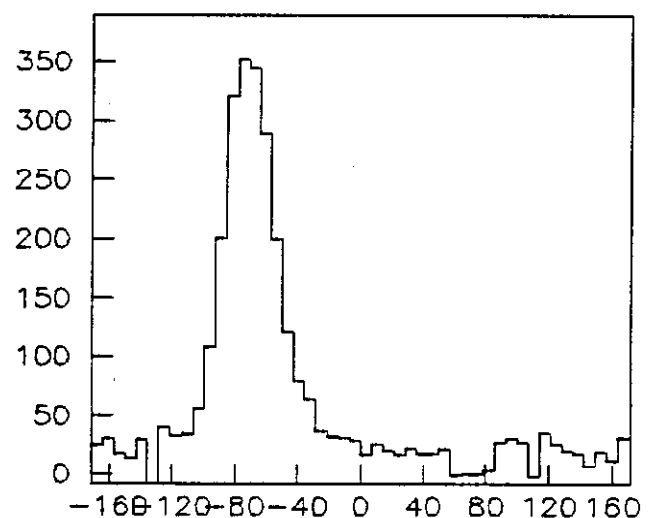
## HORZ 1 MM HORZ SPOT



## VERT 3 MM HORZ SPOT



## HORZ 3 MM HORZ SPOT

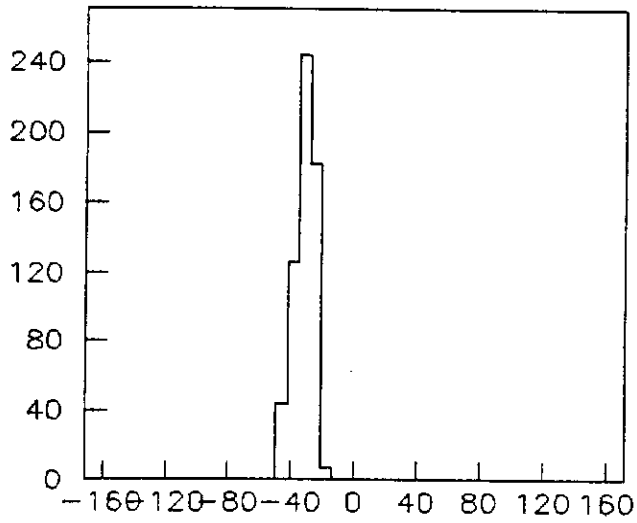


## VERT DATA

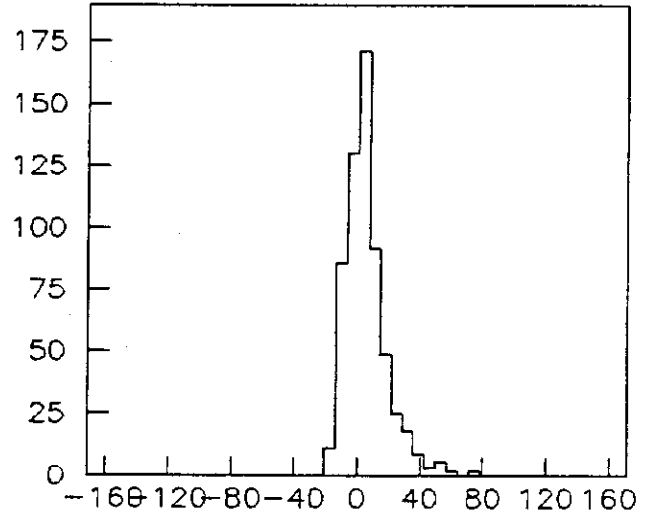
## HORZ DATA

Figure 16 b.

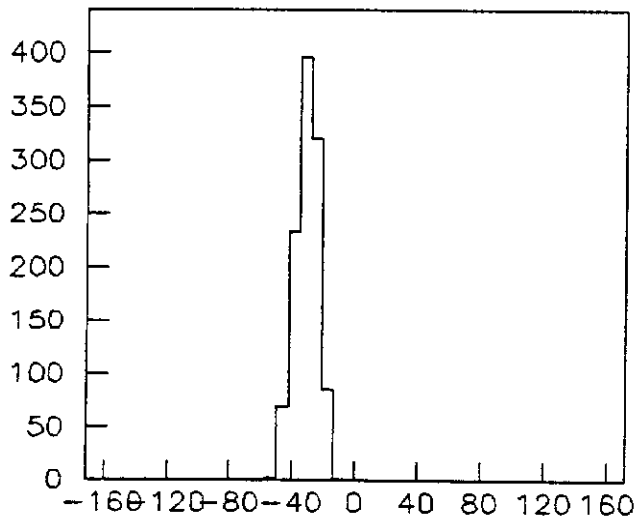
BOTTOM CENTER SECTION



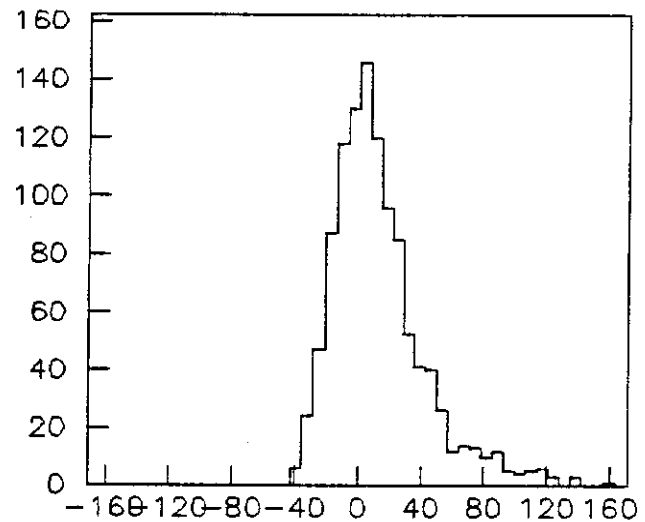
VERT 1 MM HORZ SPOT



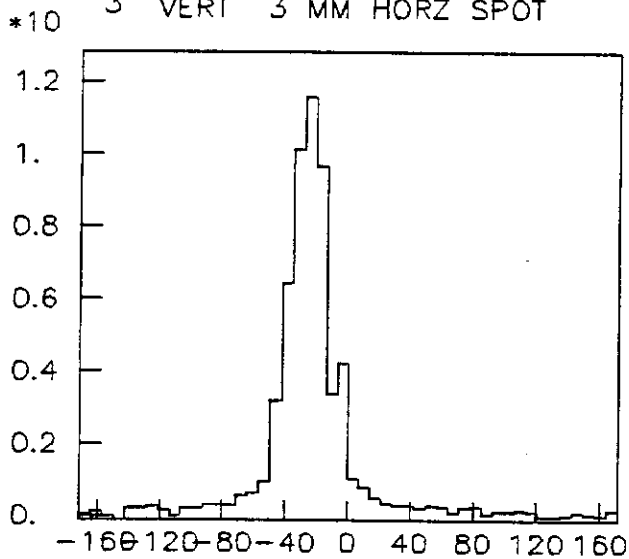
HORZ 1 MM HORZ SPOT



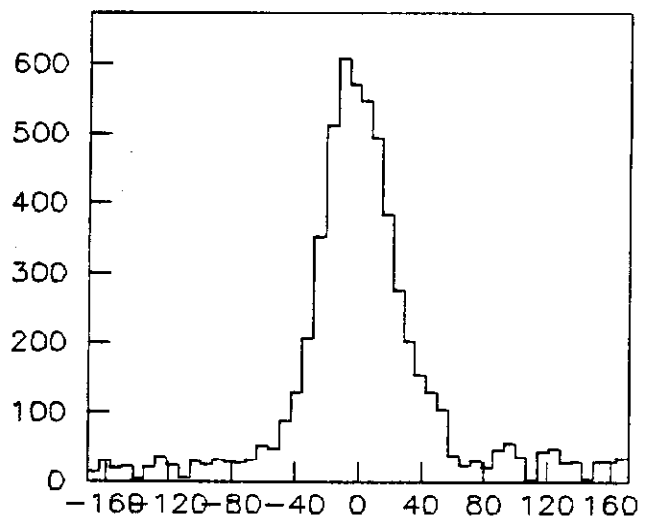
3 VERT 3 MM HORZ SPOT



HORZ 3 MM HORZ SPOT

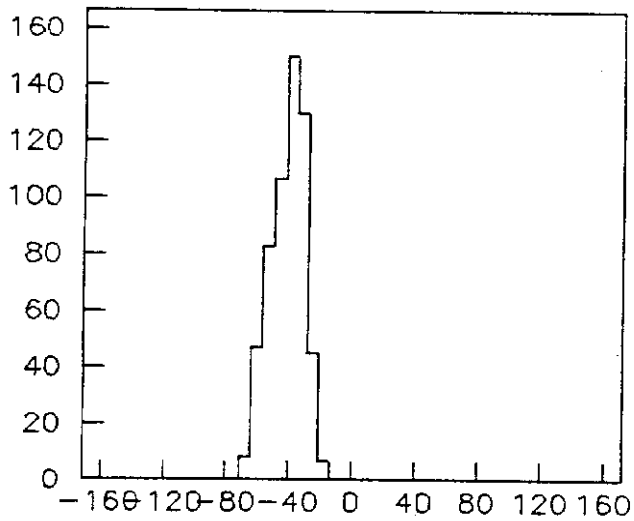


VERT DATA

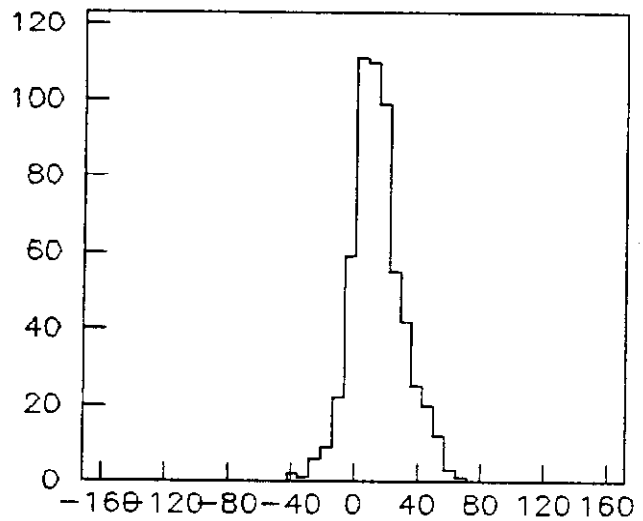


HORZ DATA

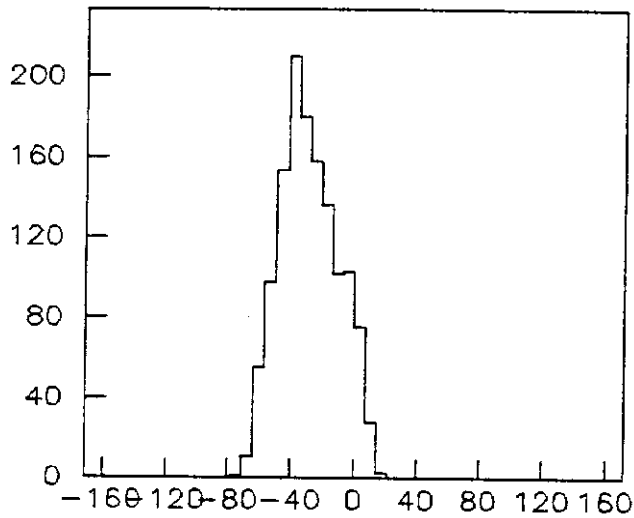
## BOTTOM WEST SECTION



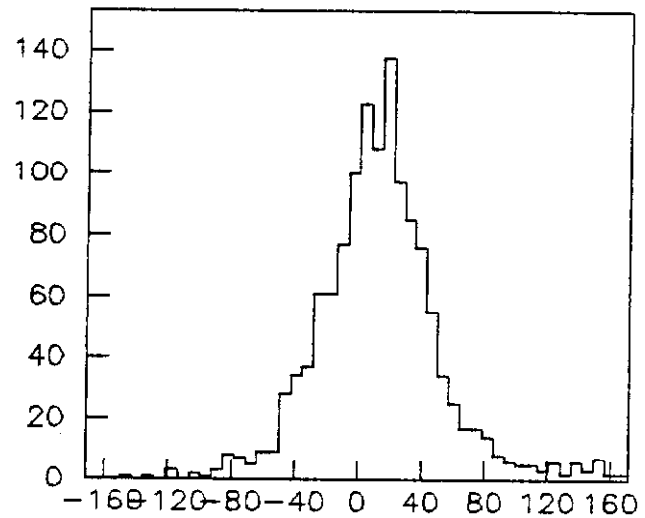
VERT 1 MM HORZ SPOT



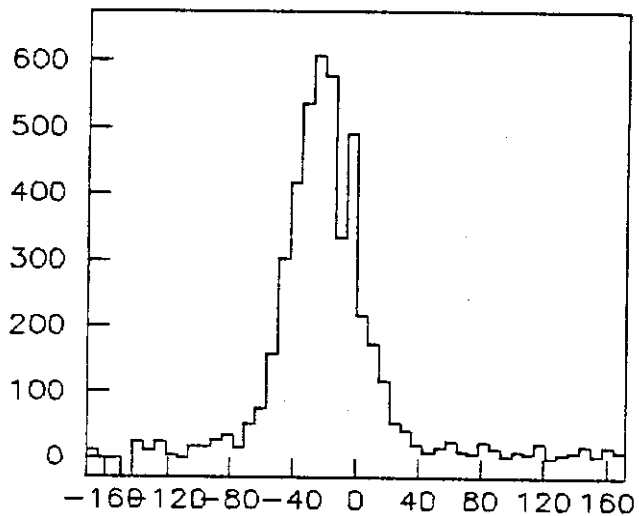
HORZ 1 MM HORZ SPOT



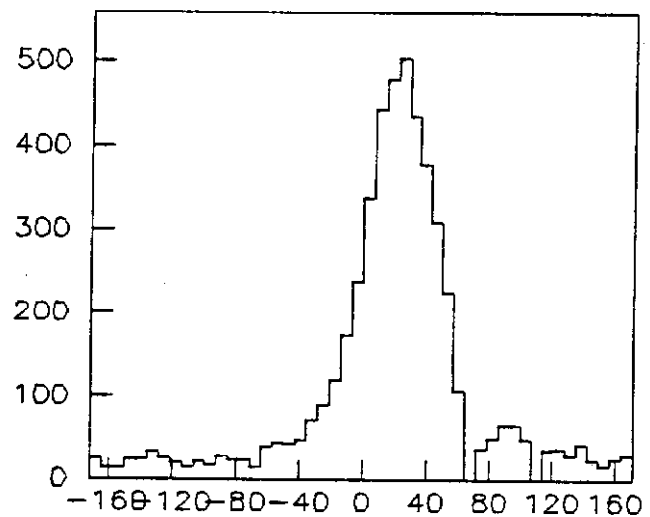
VERT 3 MM HORZ SPOT



HORZ 3 MM HORZ SPOT

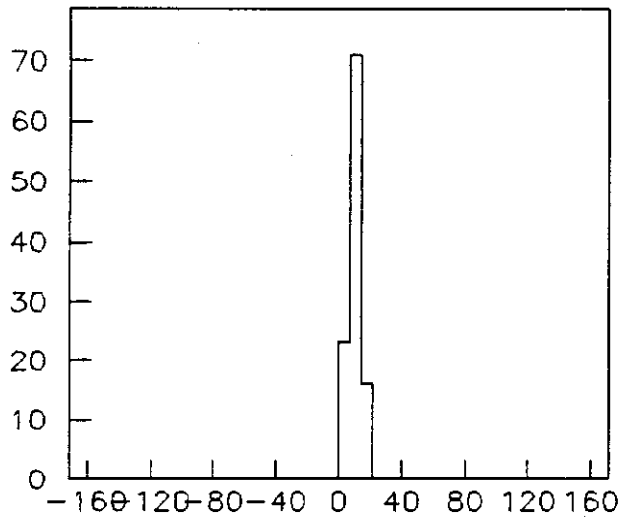


VERT DATA

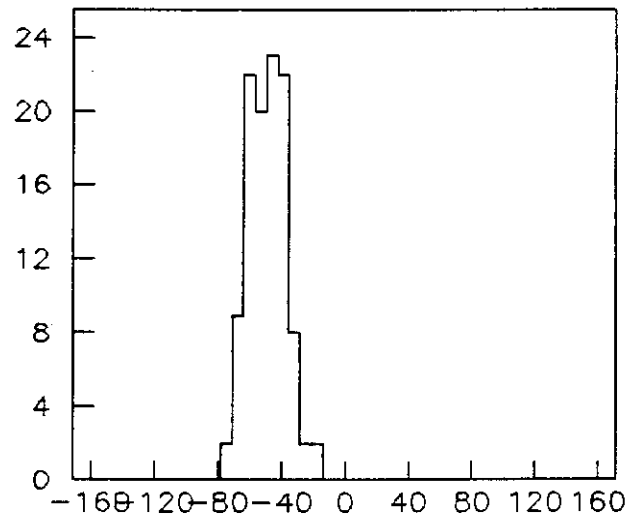


HORZ DATA

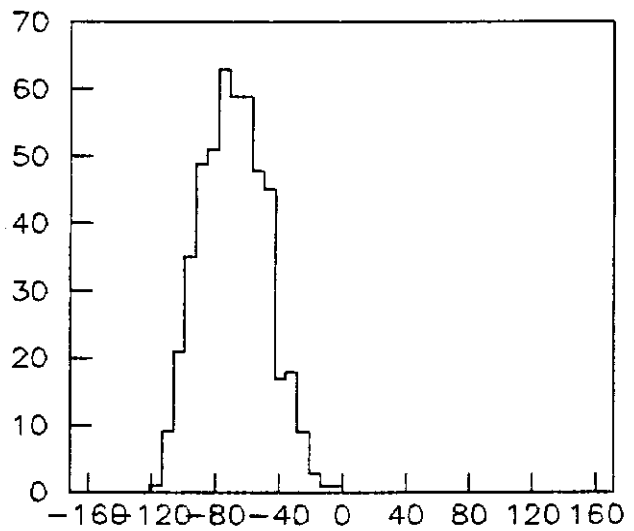
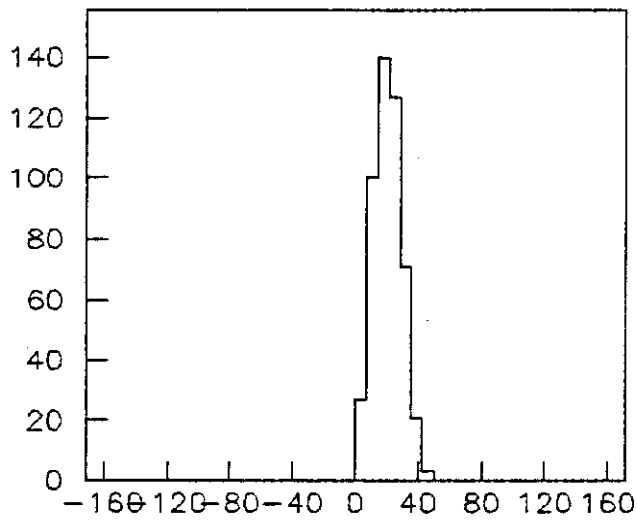
## CENTER EAST SECTION



VERT 1 MM HORZ SPOT

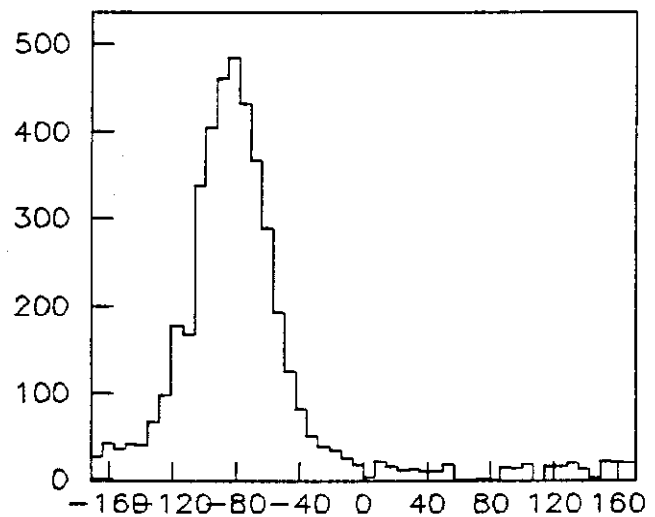
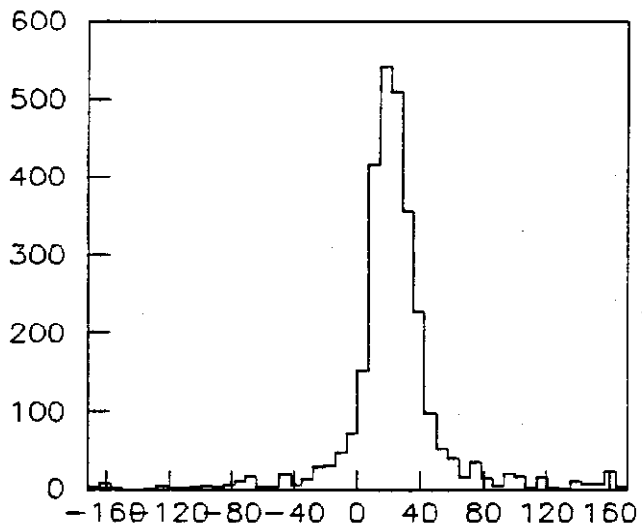


HORZ 1 MM HORZ SPOT



VERT 3 MM HORZ SPOT

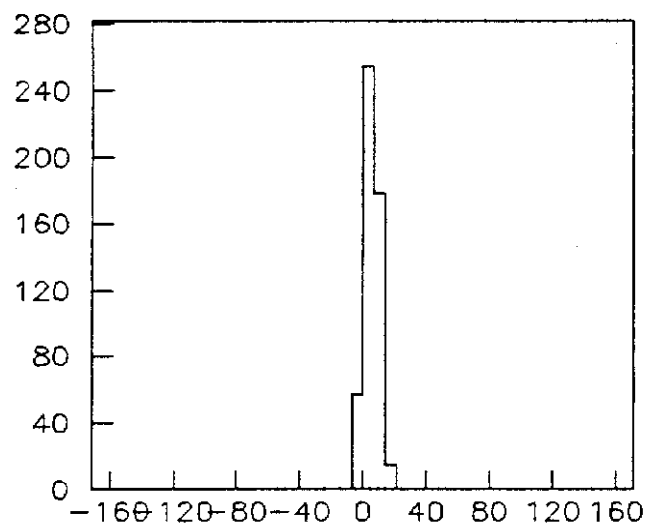
HORZ 3 MM HORZ SPOT



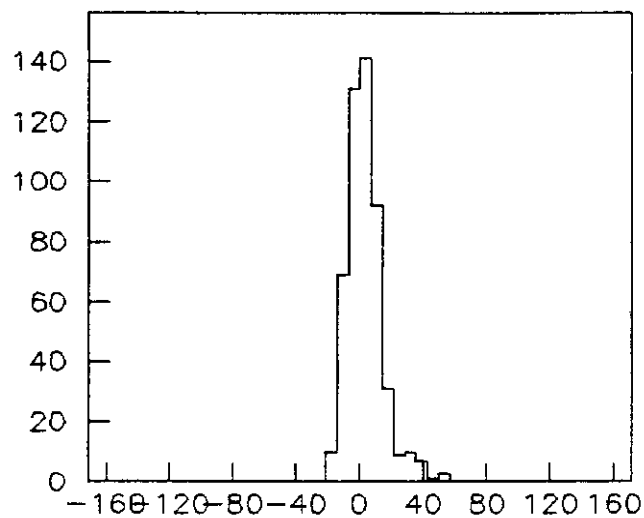
VERT DATA

HORZ DATA

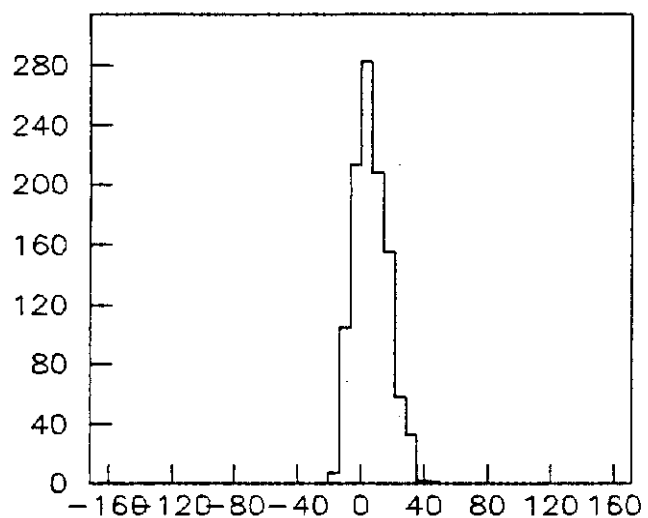
## CENTER CENTER SECTION



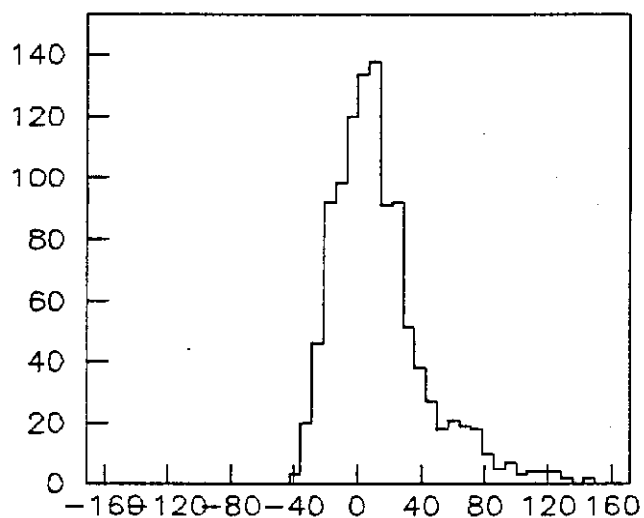
VERT 1 MM HORZ SPOT



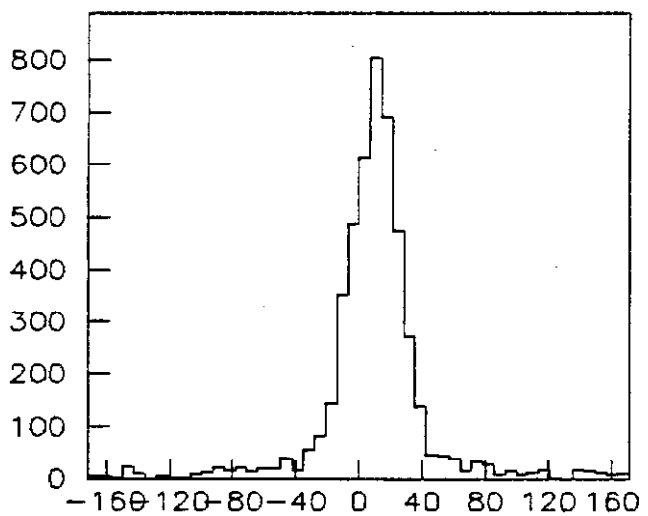
HORZ 1 MM HORZ SPOT



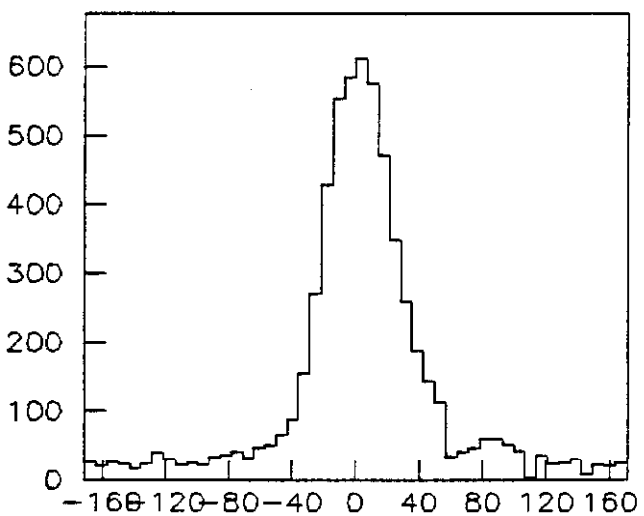
VERT 3 MM HORZ SPOT



HORZ 3 MM HORZ SPOT

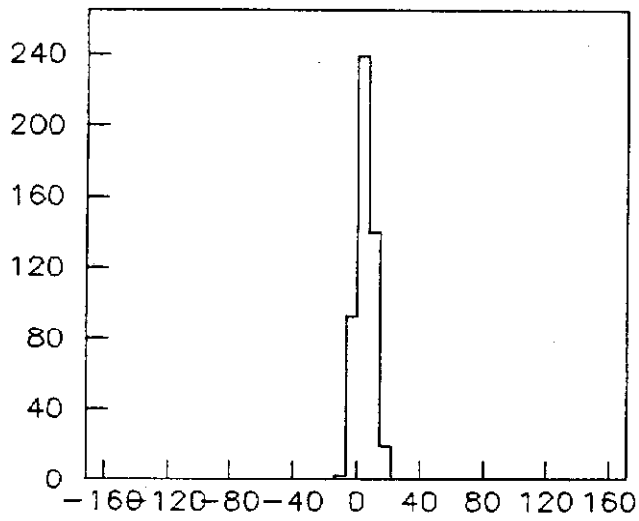


VERT DATA

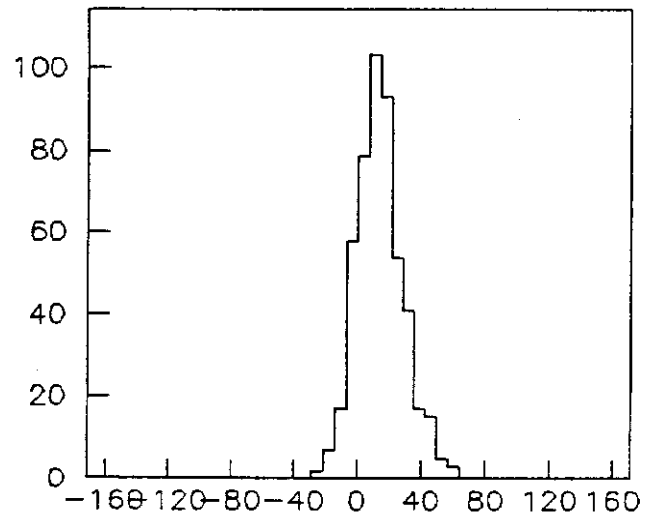


HORZ DATA

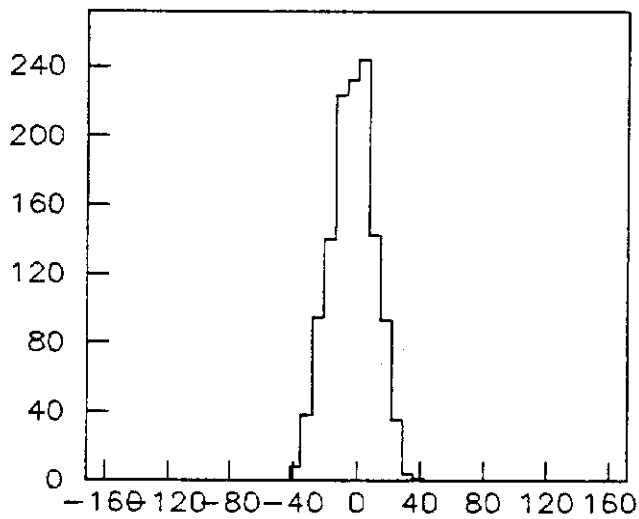
## CENTER WEST SECTION



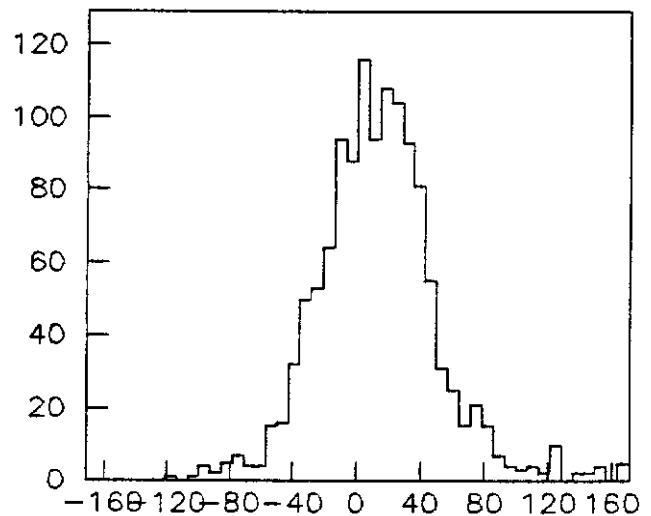
VERT 1 MM HORZ SPOT



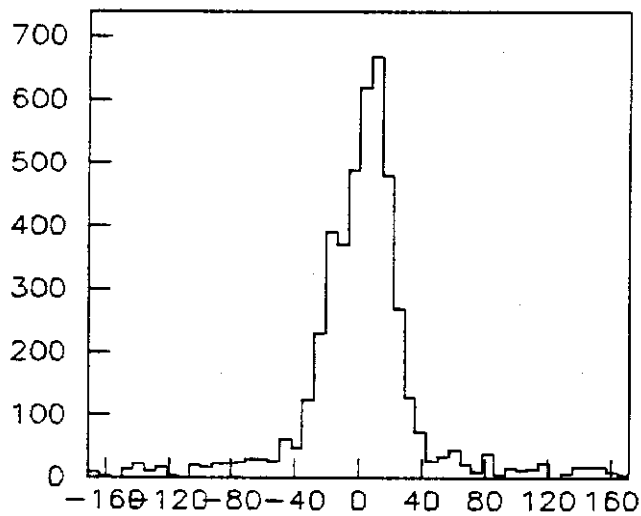
HORZ 1 MM HORZ SPOT



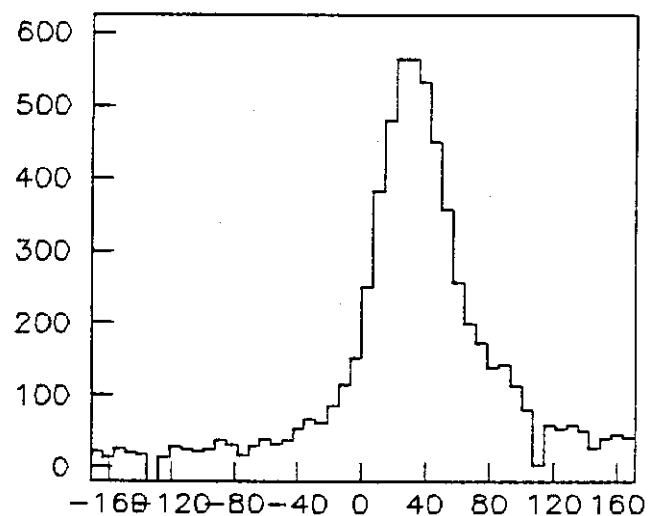
VERT 3 MM HORZ SPOT



HORZ 3 MM HORZ SPOT

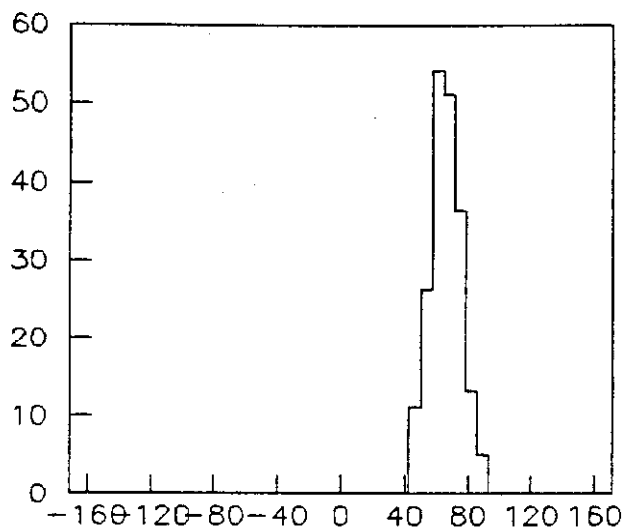


VERT DATA

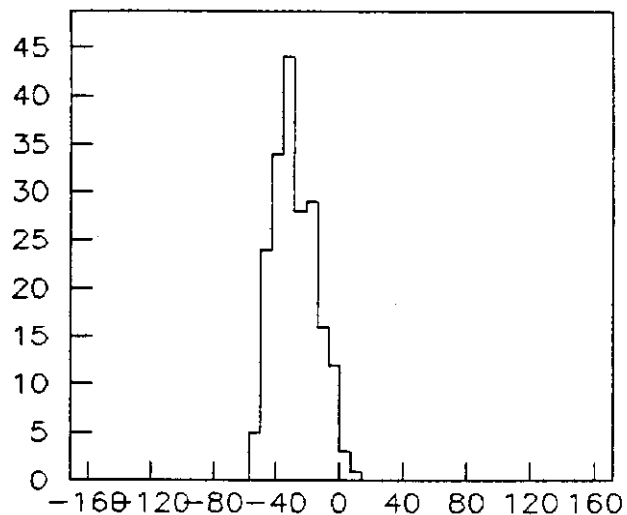


HORZ DATA

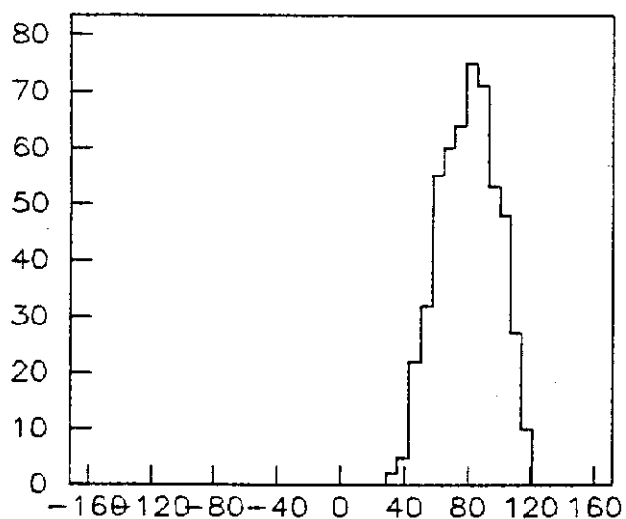
## TOP EAST SECTION



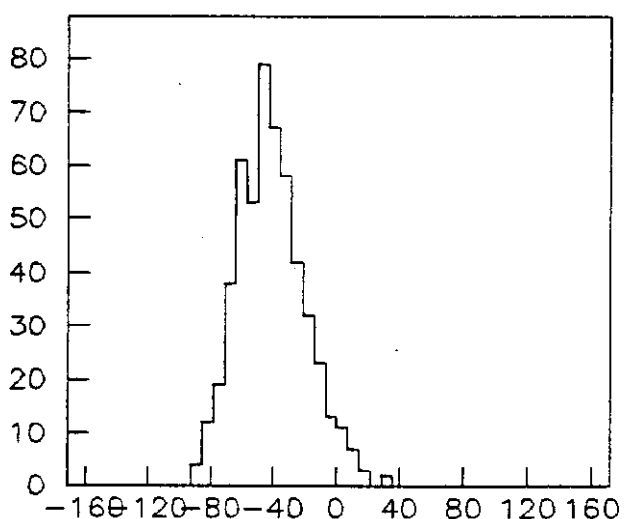
VERT 1 MM HORZ SPOT



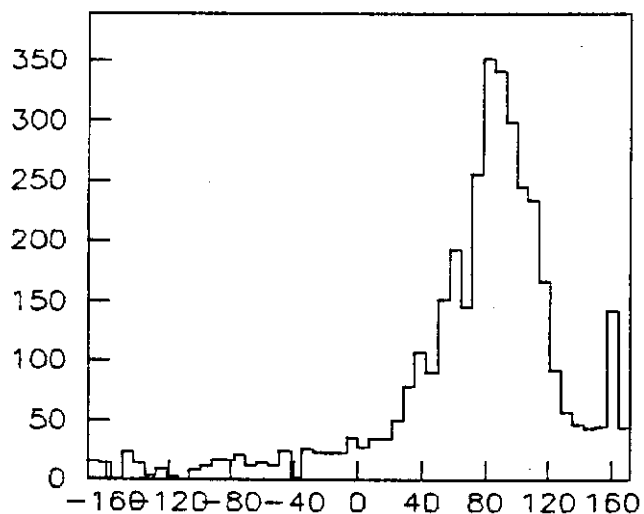
HORZ 1 MM HORZ SPOT



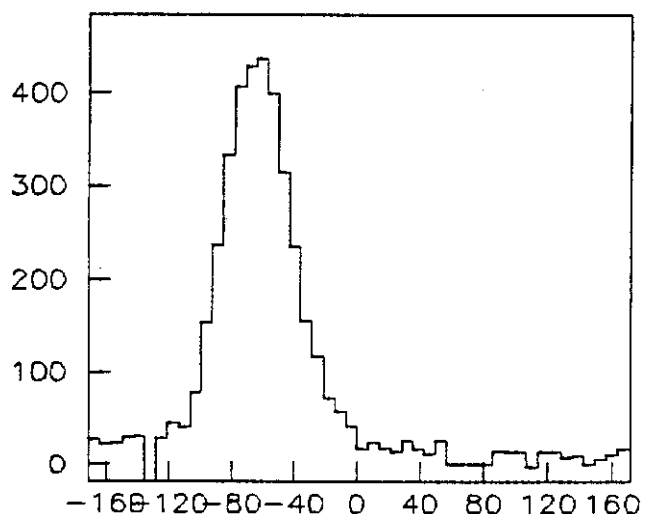
VERT 3 MM HORZ SPOT



HORZ 3 MM HORZ SPOT

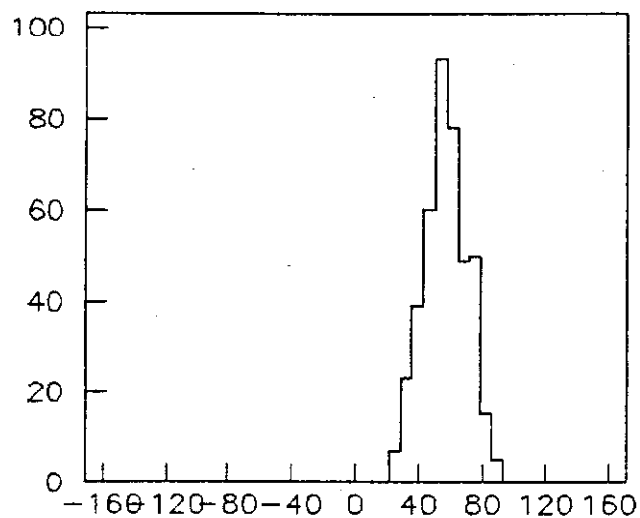


VERT DATA

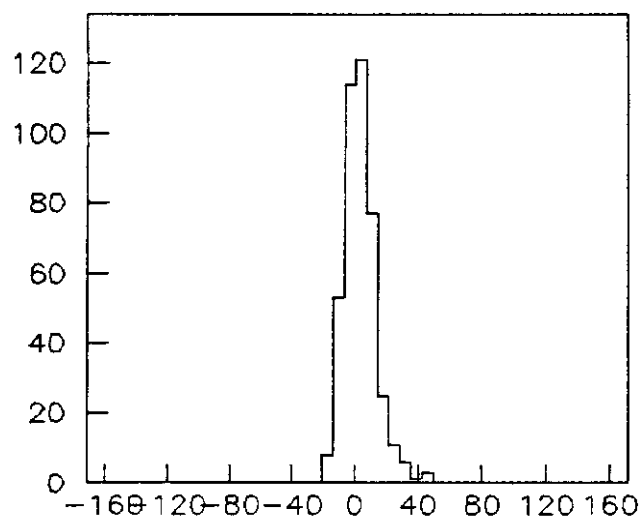


HORZ DATA

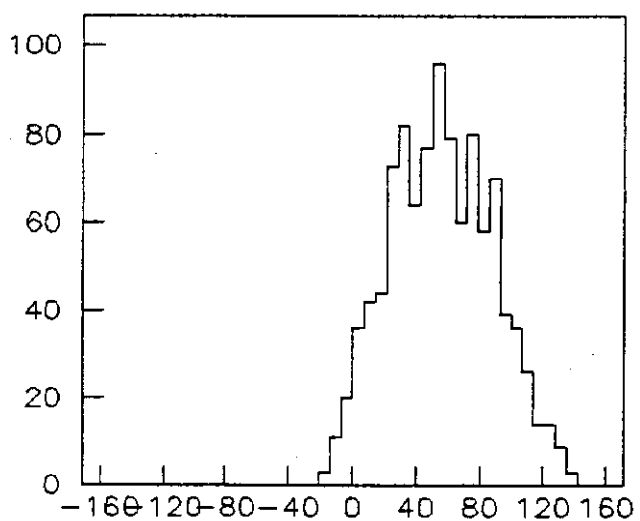
## TOP CENTER SECTION



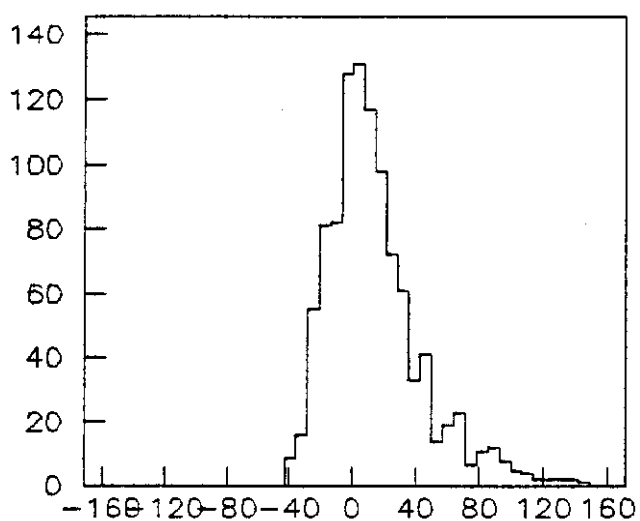
VERT 1 MM HORZ SPOT



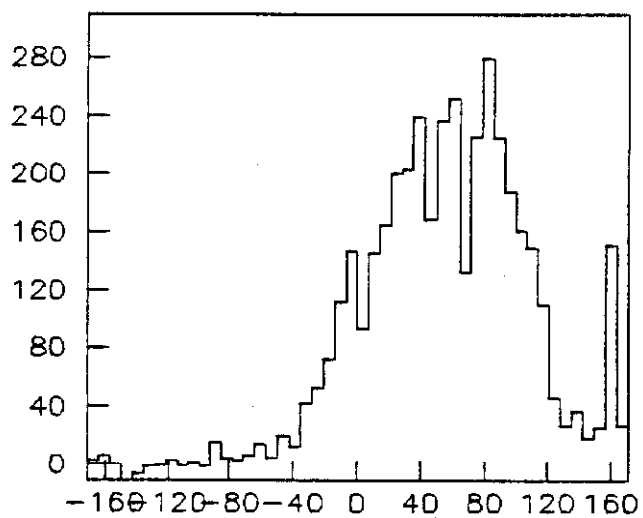
HORZ 1 MM HORZ SPOT



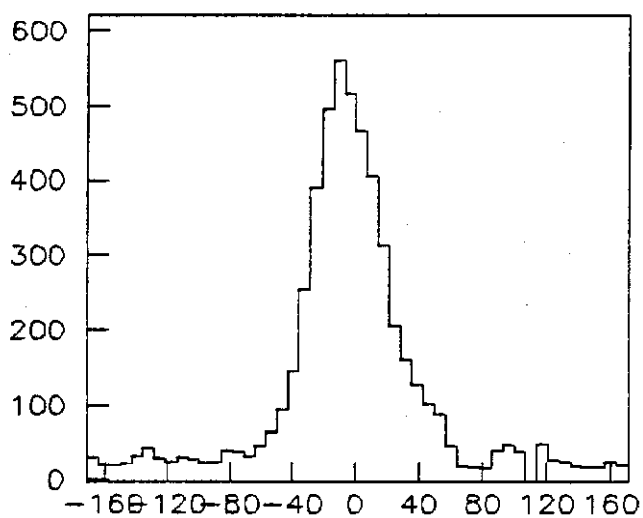
VERT 3 MM HORZ SPOT



HORZ 3 MM HORZ SPOT



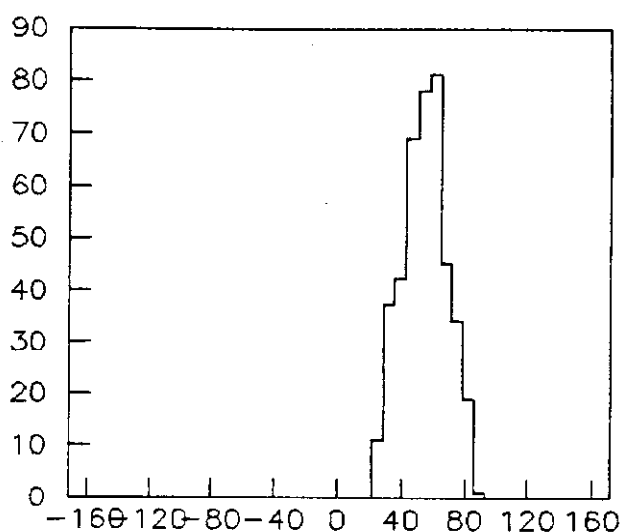
VERT DATA



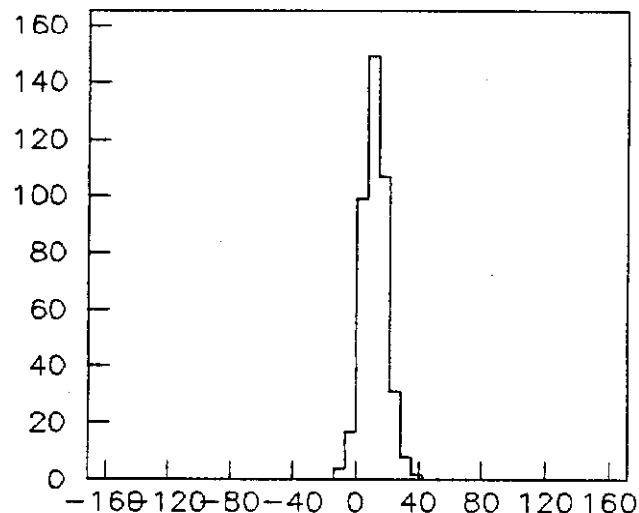
HORZ DATA



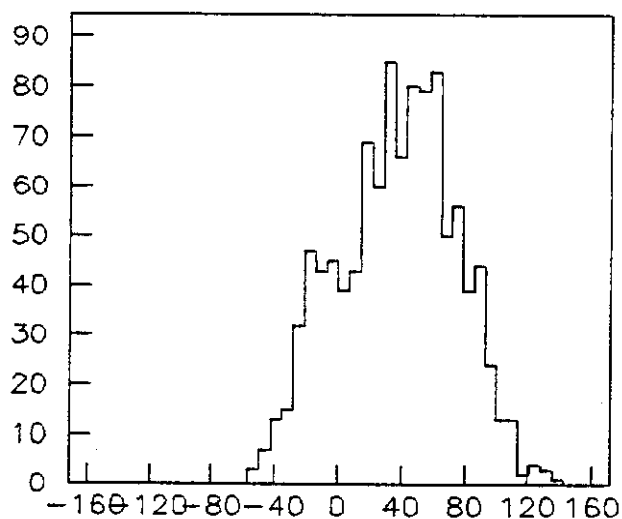
## TOP WEST SECTION



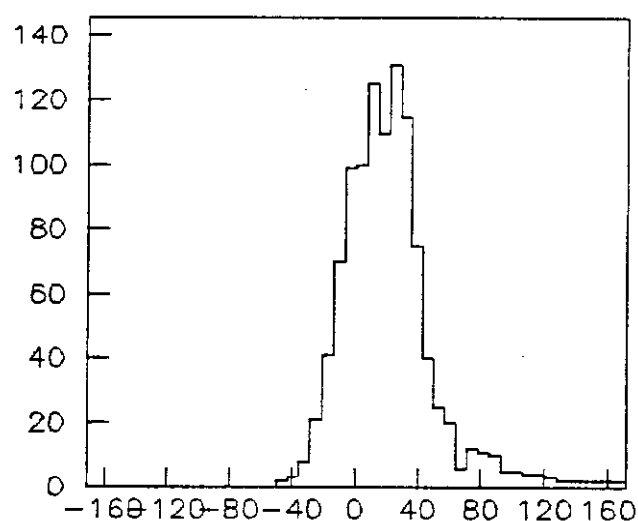
VERT 1 MM HORZ SPOT



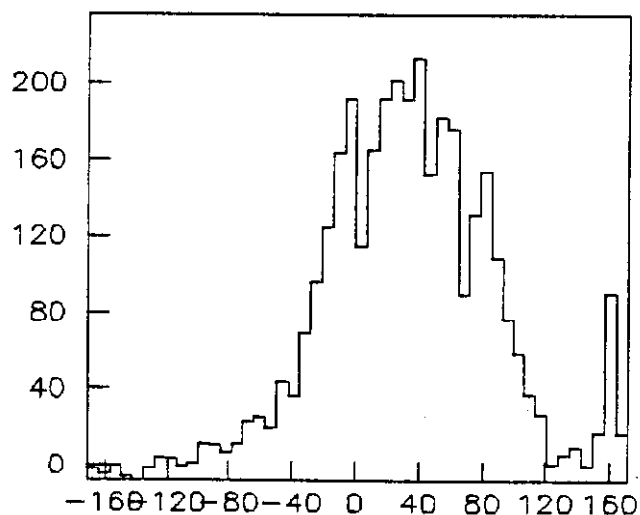
HORZ 1 MM HORZ SPOT



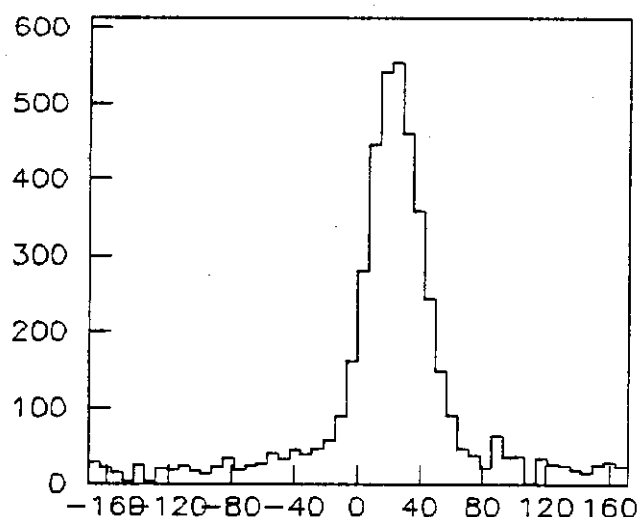
VERT 3 MM HORZ SPOT



HORZ 3 MM HORZ SPOT

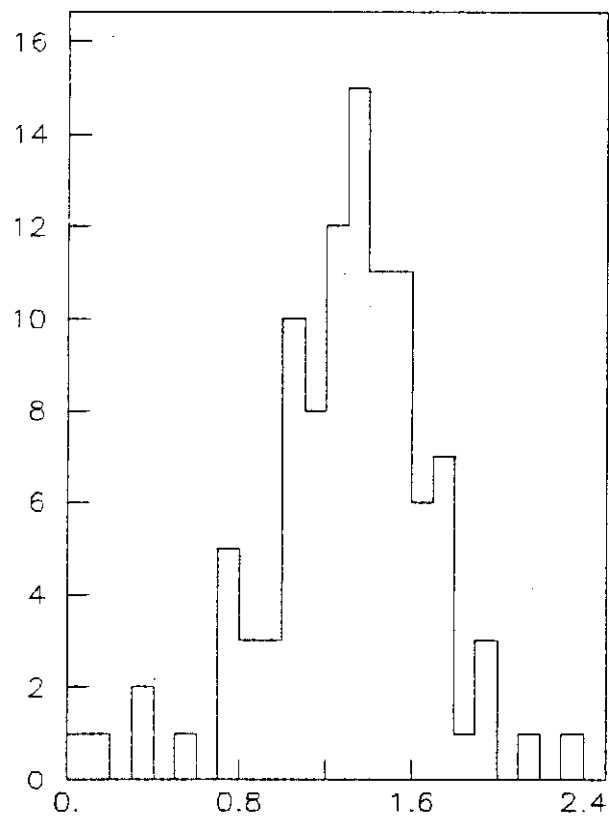


VERT DATA

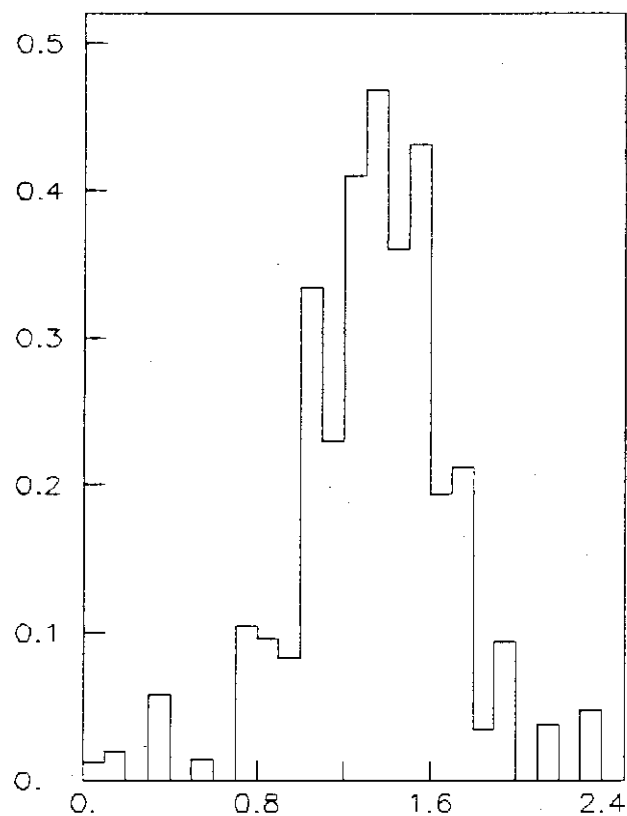


HORZ DATA

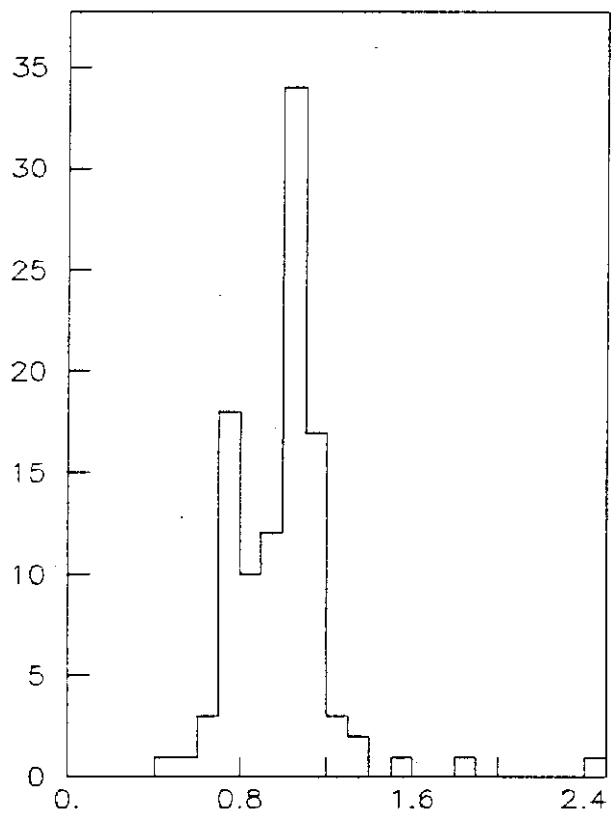
## RATIO OF SIGMAS FOR 3 MM MONTE CARLO



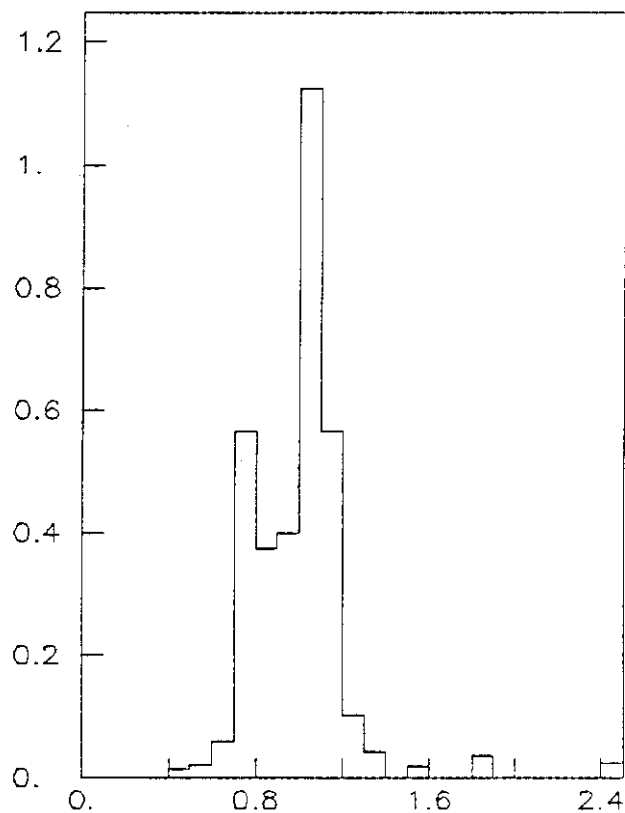
VERT DATA/MC SUM



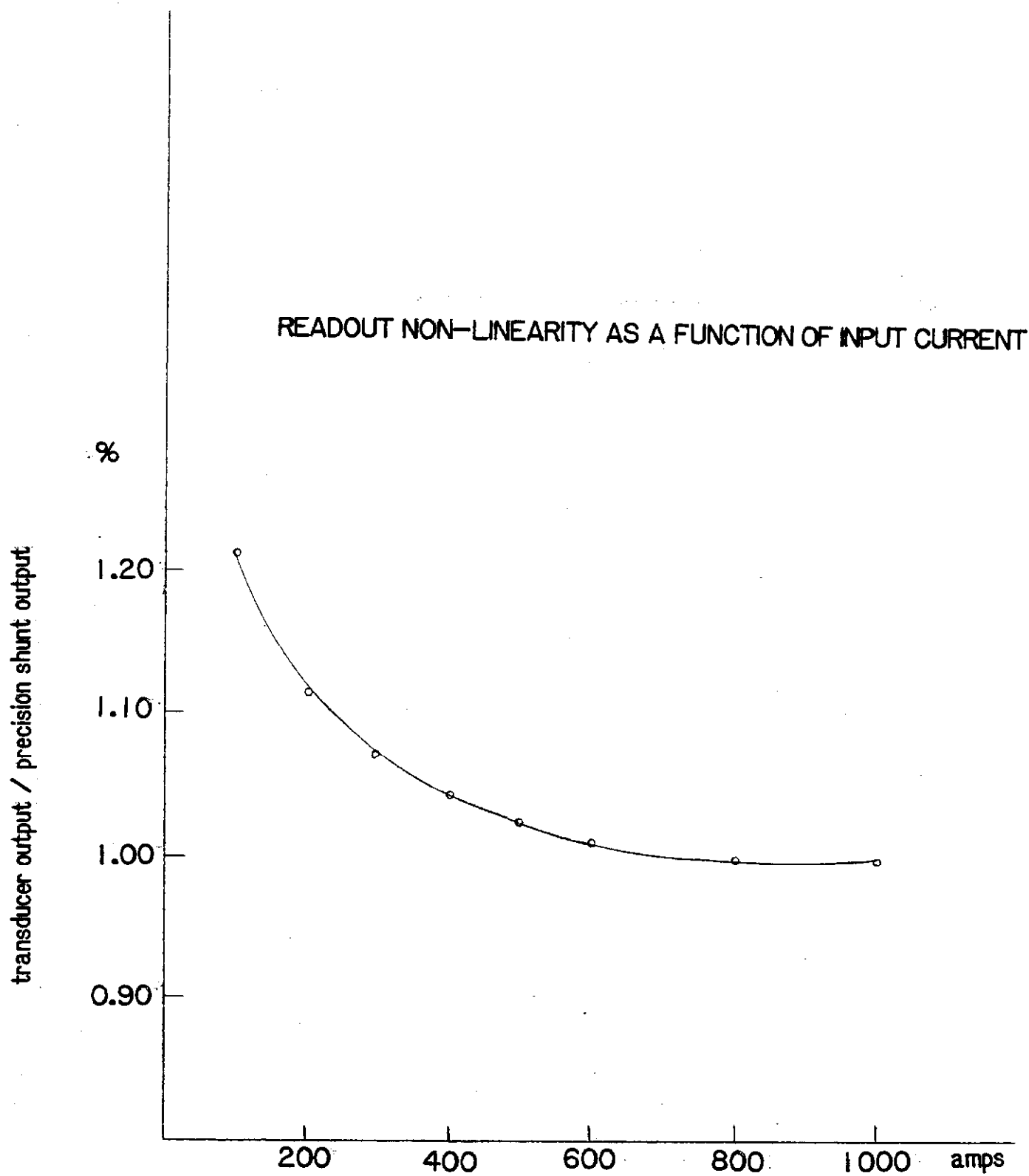
VERT DATA/MC WEIGHTED SUM



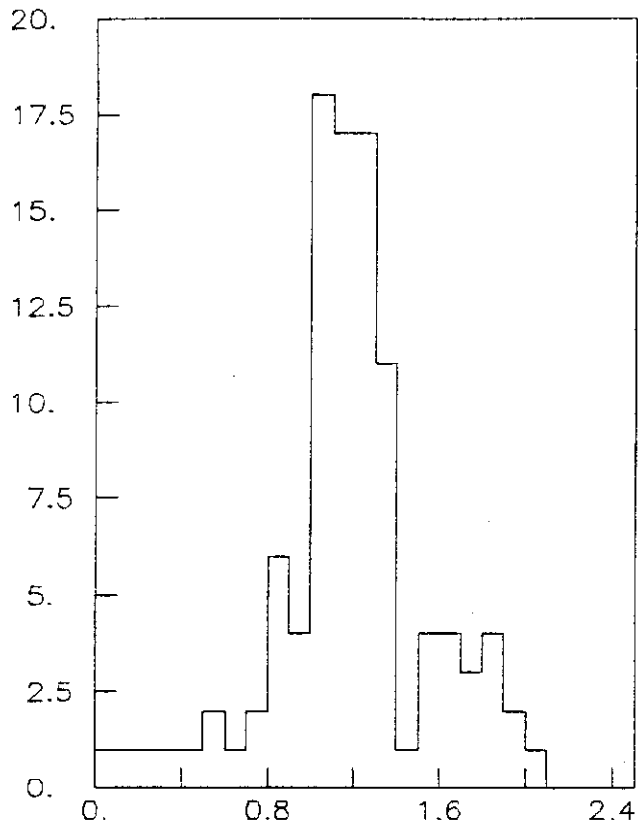
HORZ DATA/MC SUM



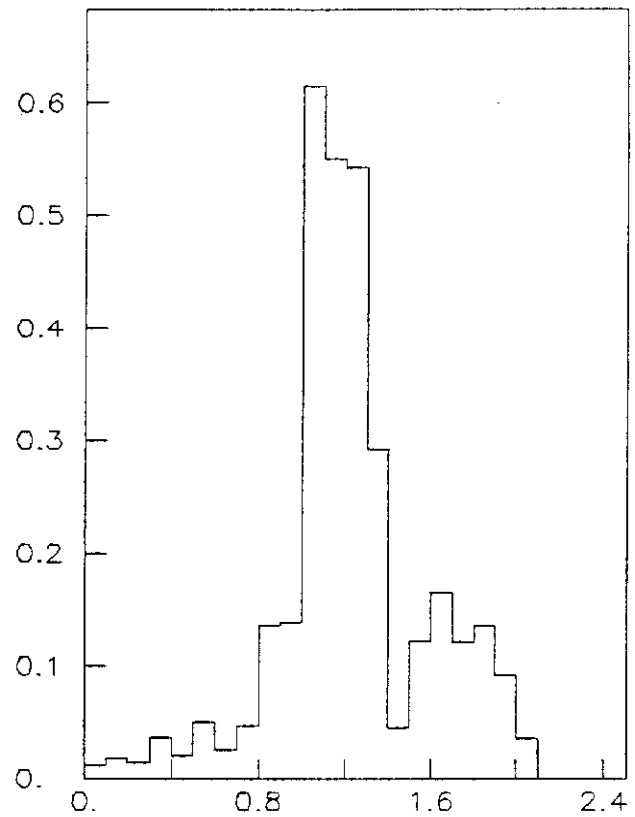
HORZ DATA/MC WEIGHTED SUM



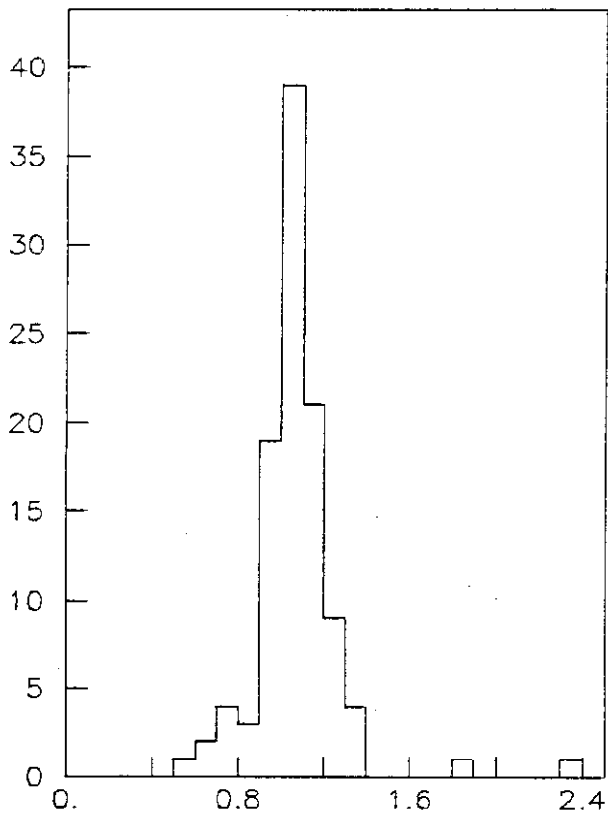
## RATIO OF SIGMAS FOR -7.5 Q4, 3 MM MONTE CARLO



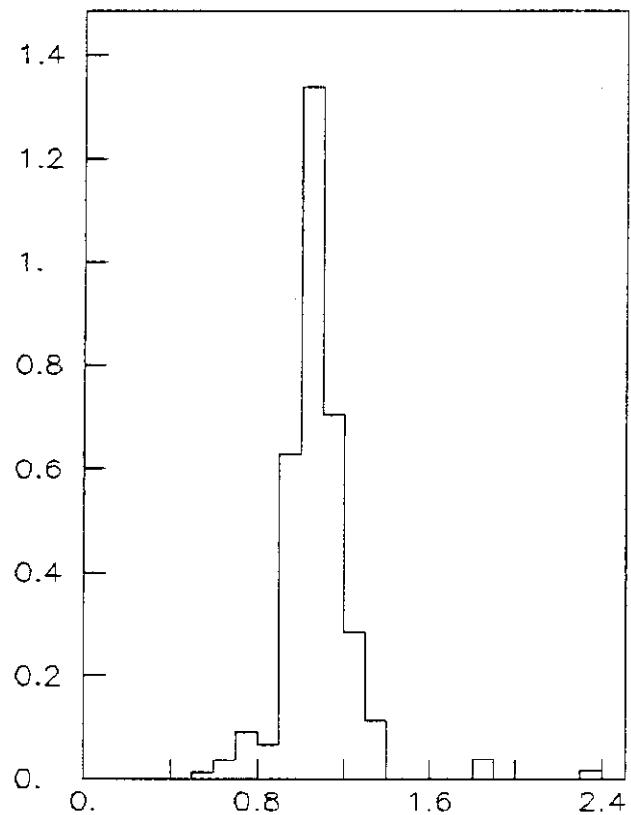
VERT DATA/MC SUM



VERT DATA/MC WEIGHTED SUM



HORZ DATA/MC SUM



HORZ DATA/MC WEIGHTED SUM